Progress in Earth and Planetary Science

REVIEW

Open Access

Progress and application of the synthesis of trans-oceanic tsunamis

Shingo Watada[1*]

Abstract

Abundant high-quality distant tsunami records from the 2010 Maule (Chile) and 2011 Tohoku-Oki earthquakes have revealed two distinctive features compared to long-wave tsunami simulations. The records show that the traveltime delay of the tsunami increases with distance from the earthquakes, and the initial phase reversal of tsunamis appears and grows systematically. The conventional tsunami theory cannot explain the observed waveforms and traveltimes of distant tsunamis, leading to the need for a new theory to explain and synthesize distant tsunamis. The propagating elevated sea surface of a tsunami compresses seawater and deforms the seafloor and the solid Earth. A propagating tsunami changes the mass distribution of the Earth and results in a spatiotemporal change in gravity, thereby altering the propagating tsunami itself. Incorporating these physics, we developed a new tsunami propagation theory in which a tsunami is naturally treated as a wave in a gravitationally and elastically coupled Earth system composed of solid Earth layers and an ocean layer. Two distinct tsunami simulation techniques based on the new tsunami propagation theory were introduced and confirmed to produce nearly identical tsunami waveforms. One technique treats tsunamis as free waves within a deformable Earth system, while the other treats tsunamis as external pressure and gravitational forces acting on the surface of a deformable Earth system. With the new techniques, the waveform and traveltime differences between the observed and simulated distant tsunamis disappear. Past distant tsunamis recorded by coastal tide gauges, which were not previously studied due to the traveltime and waveform mismatch problems, have become the focus of quantitative tsunami studies analyzing waveforms. New tsunami propagation techniques have been applied to the analysis of distant tsunami waveforms from the past 19 events and have helped to unveil the slip distributions of the past large earthquakes and to determine the earthquake origin time of the trans-Pacific tsunami events recorded by tide gauges since 1854.

Keywords Trans-oceanic tsunami, Historical tsunamis recorded in tide gauge, Tsunami in the gravitationally coupled Earth system, Tsunami phase delay, Tsunami traveltime delay, Tsunami in the deformable Earth, Earthquake fault parameters studied by tsunami waveforms, Tsunami simulation by the phase correction method, Eulerian and Lagrangian variables, Free oscillation and forced oscillation of the Earth with an ocean layer, Compressible density-stratified ocean

1 Introduction

1.1 Background on tsunami theory

Traditionally, a tsunami has been treated as a surface gravity wave of homogeneous, incompressible seawater traveling over a rigid ocean-bottom topography under constant gravity (e.g., Dingemans 1997a). When the wavelength is much longer than the water depth, as is often the case with tsunamis excited by large earthquakes (magnitude of > M8) under the seafloor, the tsunami is considered as a long

*Correspondence:
Shingo Watada
watada@eri.u-tokyo.ac.jp
[1] Earthquake Research Institute, The University of Tokyo, 1-1-1 Yayoi, Bunkyo-ku, Tokyo 113-0032, Japan

wave. Long waves are non-dispersive, meaning that the traveling speed is independent of the wavelength and wave period. As the wavelength becomes comparable to or less than the ocean depth, the surface gravity wave becomes dispersive, with longer wavelengths traveling faster.

In the real Earth, the seafloor is not rigid, but is deformable by seawater loading. Seawater is a compressible fluid because the sound waves of seawater propagate at a finite speed. The motion of the water mass and the deformation of the seafloor associated with a propagating tsunami change the distribution of the Earth's mass, causing gravity to change in space and time. Seawater compressibility and elastic deformation effects are often treated as two independent issues in tsunami propagation.

Matsuzawa (1950) simultaneously incorporated seawater compressibility and elastic deformation effects in the tsunami propagation theory for a homogeneous compressible water layer and a deformable seafloor. Nakamura (1961) plotted dispersion curves for phase and group velocities, demonstrating that the combined effects of compressible seawater and elastic seafloor in a 4.5 km deep ocean reduce the maximum tsunami phase and group velocities by 1%. However, these early works were largely unnoticed by the tsunami research community until we re-discovered them after the 2011 Tohoku-Oki earthquake tsunami.

1.1.1 Compressibility and density stratification of seawater

Eckart (1960), Stoneley (1963), and Sells (1965) discussed surface gravity waves in a slightly compressible ocean. Incorporating the compressibility of seawater under gravity automatically implies the water is density-stratified, i.e., no longer homogeneous. The three studies mentioned assumed that the compressible seawater stratifies adiabatically. Density stratification of water always slows down the long-wave speed (e.g., Watada 2013), i.e., when the total thickness of the density-stratified water is d, then the long-wave speed is smaller than $\sqrt{gd}$, where g is the gravity.

Watada (2013) developed a propagator matrix theory that can be used to compute the wave motion and dispersion relation for arbitrarily stratified compressible seawater under gravity. For a constant-depth water layer with density scale height H and sound velocity c_s, the theory gives an explicit formula for the phase velocity of a surface gravity wave with horizontal wavenumber k and angular frequency ω propagating at phase velocity $c_p = \omega/k$. The formula is expressed as:

$$c_p^2(\omega, k) = \frac{\omega^2}{k^2} = d\left(g - \frac{\omega^2}{2k^2H}\right)\frac{\tanh(Md)}{Md} \tag{1}$$

where

$$M^2(k,\omega) = k^2\left(1 - \frac{\omega^2}{k^2c_s^2}\right)\left(1 - \frac{N^2}{\omega^2}\right) + \Gamma^2 \tag{2}$$

$$N^2(z) = -g\left(\frac{1}{\rho_o}\frac{d\rho_0}{dz} + \frac{g}{c_s^2}\right) = \frac{g}{H} - \frac{g^2}{c_s^2} \tag{3}$$

$$\Gamma(z) = \frac{1}{2\rho_0}\frac{d\rho_0}{dz} + \frac{g}{c_s^2} = -\frac{1}{2H} + \frac{g}{c_s^2} \tag{4}$$

$$\rho_0(z) = \rho_{0b}\exp\left(-\frac{z}{H}\right) \tag{5}$$

z is the upward positive vertical coordinate, N is the buoyancy frequency, $N^2 \geq 0$ implies that the layer is stably stratified, while $N^2 < 0$ implies that the layer is unstable and cannot stably exist in nature. ρ_o is the stratified water density at rest. ρ_{0b} is the water density at the bottom of the layer. Equation 1 serves as a basic dispersion relation, from which the dispersion relations for various water layer cases are obtained. It should be noted that Eq. 1 does not depend on the magnitude of ρ_o but on the gradient of density $d\rho_0/dz$. In the simplest case, where water is incompressible ($c_s = \infty$) and homogeneous ($H = \infty$), we confirm that the well-known surface gravity wave dispersion relation is obtained.

$$c_p^2 = \frac{\omega^2}{k^2} = gd\frac{\tanh(kd)}{kd} \tag{6}$$

For a constant density layer with finite compressibility, although such a layer is unstable ($N^2 \leq 0$), the phase velocity (Eq. 1) of a long wave is reduced to:

$$c_p \approx \sqrt{gd\left(1 - \frac{\omega^2}{3k^2c_s^2}\right)} \approx \sqrt{gd}\left(1 - \frac{gd}{6c_s^2}\right) \tag{7}$$

Okal (1982) also obtained the reduced long-wave phase velocity of Eq. 7 by applying the normal mode theory to a spherical Earth, in which an ocean layer is modeled as a homogeneous water layer. For an adiabatically density-stratified layer with finite compressibility, the phase velocity (Eq. 1) of a long wave is reduced to:

$$c_p \approx \sqrt{gd\left(1 - \frac{\omega^2}{2k^2c_s^2}\right)} \approx \sqrt{gd}\left(1 - \frac{gd}{4c_s^2}\right) \tag{8}$$

Both Sells (1965) and Tsai et al. (2013) obtained the same reduced long-wave phase velocity in Eq. 8. Wang (2015) derived a reduced long-wave phase velocity for compressible seawater as:

$$c_p \approx \sqrt{gd\left(1-\frac{\omega^2}{k^2c_s^2}\right)} \approx \sqrt{gd}\left(1-\frac{gd}{2c_s^2}\right) \tag{9}$$

Stoneley (1963) also obtained Eq. 9. The long-wave speed reduction in Eq. 9 is twice as large as that in Eq. 8. Sells (1965) pointed out errors in Stoneley (1963) that cause Stoneley's speed reduction estimate to be twice as large as Sells's estimate. It should be noted that the long-wave speed reduction caused by density stratification and compressibility of seawater is independent of wave period and the wavelength (Sect. 2.5.1).

Wang (2015) justified the use of Eq. 9 for distant tsunami traveltime calculations by comparing the observed traveltime delay without taking account of the elastic deformation of the seafloor. The apparent coincidence between traveltime delays based on Eq. 9 and the observed delays is due to two errors: an overestimation of the compressibility effect and neglecting the elastic deformation and gravitational perturbation effects (which are discussed in Sects. 1.1.2, 1.1.3, 2.5.2, and 2.5.3), partially cancel each other out. Based on Eq. 9, Wang (2015) proposed a depth-correction scheme for computing tsunami traveltimes. Inazu and Saito (2013) proposed a similar depth correction approach in which the depth correction factor to fit the observed traveltime delays was empirically determined. Wang et al. (2022) proposed an extended depth-correction scheme. All depth-correction schemes do not alter the non-dispersive nature of long waves and only adjust the traveltimes. Therefore, these depth-correction schemes do not reproduce the observed waveforms of distant tsunamis, particularly the initial phase reversal, as discussed in Sect. 2.2. The polarity of the initial phase of a tsunami is critical for tsunami source studies (Sect. 2.1). Depth-correction schemes can be used for tsunami warning studies, which do not require the accurate forecasting of tsunami waveforms and arrival times.

Watada (2013) computed the tsunami traveling speed by using the propagator matrix method at all global ocean grid points where the vertical density and sound velocity profiles were available. In general, the tsunami travel speed reduction is larger in deeper oceans (Eq. 8), with small deviations depending on the local variations of the density and sound velocity vertical profiles. At a depth of 4 km, density stratification reduces the tsunami speed by 0.15% and the compressibility of homogeneous seawater additionally reduces by 0.3%, leading to a total reduction of ~ 0.44%. However, the speed reduction due to compressible seawater alone is insufficient to account for the observed traveltime delay in the far field, which is ~ 1–1.5% (Sect. 1.2).

1.1.2 Elastic deformation of seafloor

The effect of seafloor deformation on tsunami propagation was studied by Mallard and Dalrymple (1977) for a homogeneous incompressible water layer over a homogeneous elastic half-space, without the inertial term in the elastic seabed. Dawson (1978) emphasized the importance of the inertia term, especially for a thick soft bottom medium, and included it in his formulation. Yamamoto (1982) developed analytic formulas for the dispersion relation of surface gravity waves and acoustic waves in compressible homogeneous water, as well as for the excitation of a tsunami and acoustic waves by an uplift of the ocean bottom in a two-layered system. Comer (1984) computed the tsunami excitation by an earthquake point source in a two-layered system composed of an incompressible water layer and an elastic half-space.

Tsai et al. (2013) derived the dispersion relation of a tsunami for a homogeneous incompressible water layer as:

$$c_p = \sqrt{gd}\left(1-\frac{(1-\nu)\rho_0 g}{2\mu k}\right) \tag{10}$$

where ν is the Poisson's ratio and μ is the shear modulus of the elastic half-space. Note that, unlike the stratification and compressibility effects of seawater, the elasticity effect of the seafloor is wavenumber dependent and causes non-dispersive long waves to become dispersive. The tsunami phase speed decreases with increasing wavelength or wave period, i.e., reverse dispersion at long wavelengths. However, the seafloor elasticity alone cannot explain the observed far-field traveltime delays (Sect. 2.5). By combining seawater compressibility (Eq. 8) and elastic seafloor (Eq. 10), Tsai et al. (2013) obtained a dispersion relation of linear surface gravity waves for adiabatically-stratified compressible seawater and elastic ocean bottoms. Abdolali et al. (2019) also obtained the tsunami dispersion relation, including the effect of seawater compressibility and elastic seafloor.

In all studies introduced so far in this section, the gravity field is constant in space and time, as in the conventional tsunami simulation. Their tsunami simulations do not include the effect of the gravity change induced by the mass movement of seawater and the deformation of the seafloor during the tsunami propagation.

1.1.3 Gravity change

Studies of water waves often assume that the Earth's gravity is constant, both horizontally and vertically. In the spherically symmetric Earth, gravity acts in the vertical direction but its magnitude varies depending on the density structure. The time-constant background gravity

of such an Earth model varies spatially as a function of the distance from the center of the Earth, resulting in different gravity values at the top and bottom of the ocean layer. The normal mode theory of a symmetric Earth can handle non-uniform gravity fields and compute linear surface gravity waves, including non-dispersive long waves and dispersive short waves, (Ward 1980; Okal 1982; Watada and Kanamori 2010), without using the linear Boussinesq approximations often employed to compute dispersive linear water waves (e.g., Dingemans 1997b; Baba et al. 2015).

As the Earth deforms, its mass distribution changes, leading to a spatiotemporal change in the self-attracting force of gravity. This change in the Earth's gravity field, in turn, affects on the Earth's internal mass and deforms the Earth. The shape of deforming Earth is determined by the elastic stress and gravitational mass attraction force within the Earth and external loading and gravitational forces. The Earth's response to an external force, or an external gravitational potential on the Earth, is a classic subject of Earth tides (e.g., Farrell 1972). Ocean tide prediction requires solving the SAL of the moving surface water mass under the constantly changing lunar and solar gravitational forces. While modern tidal theories still assume homogeneous incompressible seawater (e.g., Sulzbach et al. 2021), the Earth's SAL deformation and gravity change during tsunami propagation in compressible seawater are incorporated into the tsunami computations in Sects. 2.5.1 and 2.6.3.

1.2 Background on tsunami observation

1.2.1 Coastal tide gauge records

Tsunami waveforms and traveltimes recorded at coastal tide gauges are strongly influenced by coastal topography and shallow bathymetry. Incomplete knowledge of the shallow water bathymetry around the tide gauge has been believed to cause differences between observed and simulated tsunamis.

A tsunami generated by the 1960 Chile earthquake was recorded in and around the Pacific Ocean. Nakamura and Watanabe (1961) reported tsunami forerunners, i.e., small-amplitude and short-period water-level oscillations preceding the arrival of a huge tsunami along the coast of Japan. They attributed the forerunner to seiches of a bay or a continental shelf near the tide gauge. Imamura et al. (1987, 1990) pointed out through numerical simulation of tsunamis that the calculated arrival times were 10 min to a few hours earlier than observed in the far field (North America, Australia, Japan, and Taiwan) as well as near field (South America). The discrepancy was attributed to the use of a coarse numerical grid and the effect of coastal topography around the observation points. Tide gauge records from the Pacific Islands, such as Christmas, Johnston, and Midway Islands (Fig. 1), although not mentioned by the authors, show a precursory phase with negative polarity before the conspicuous water-level rise (Zetler and Symons 1961).

1.2.2 Offshore tsunami records

Two types of instruments that directly record tsunami waveforms are used to eliminate the influence of coastal and shallow-water bathymetry: a buoy floating on the sea surface (Kato et al. 2005; Kawai et al. 2013) and a submarine cable laid on the seafloor (Takahashi 1981; Aoi et al. 2020).

The Ports and Harbours Bureau of MLIT and its associated organizations operate the NOWPHAS GPS wave gauge network, which records the elevation of GPS buoys every second to monitor the sea wave height. NOWPHAS installed 15 GPS wave gauges before the 2011 Tohoku-Oki earthquake and three additional ones after the earthquake. Of the 18 GPS wave gauges, three were installed off the coast of the Sea of Japan, and the rest were installed off the Pacific coast. The NOWPHAS GPS buoys are powered by solar cells. The altitude of a floating buoy is measured using GPS-RTK technology, which measures the relative position between the GPS receiver installed on a floating buoy and the GPS receiver at a land station. The nominal resolution of the three-dimensional relative position is several centimeters or more depending on the GPS satellite conditions. The GPS signals received by the floating buoy are transmitted by radio to the land station and are processed in real-time for GPS-RTK positioning. Radio transmission requires the buoy to be located within 20 km of the land station. The NOWPHAS GPS buoys are moored at water depths of 100–400 m.

The 2011 Tohoku-Oki earthquake coseismically deformed large submarine and subaerial regions in three dimensions (e.g., Ozawa et al. 2011). The relative elevation between the floating buoy and the land station changed coseismically by as much as 0.95 m (cf. Kawai et al. 2013). The modeling of tsunami waveforms recorded by GPS buoys should include such a coseismic offset of the relative elevations (e.g., Ho et al. 2017). Some early tsunami waveform studies of the 2011 Tohoku-Oki earthquake tsunami did not include the coseismic offset of GPS buoys in tsunami waveform modeling (e.g., Yamazaki et al. 2011), and systematic offsets remained in the modeling residuals.

OBPGs powered by cable and transmitting data in real-time through the cable have been the primary tsunami observation system to quickly detect the occurrence of earthquakes and tsunamis offshore Japan (Tsushima and Ohta 2014). Before the 2011 Tohoku-Oki earthquake, three (Tokai, Boso, and Tonakai) submarine cables

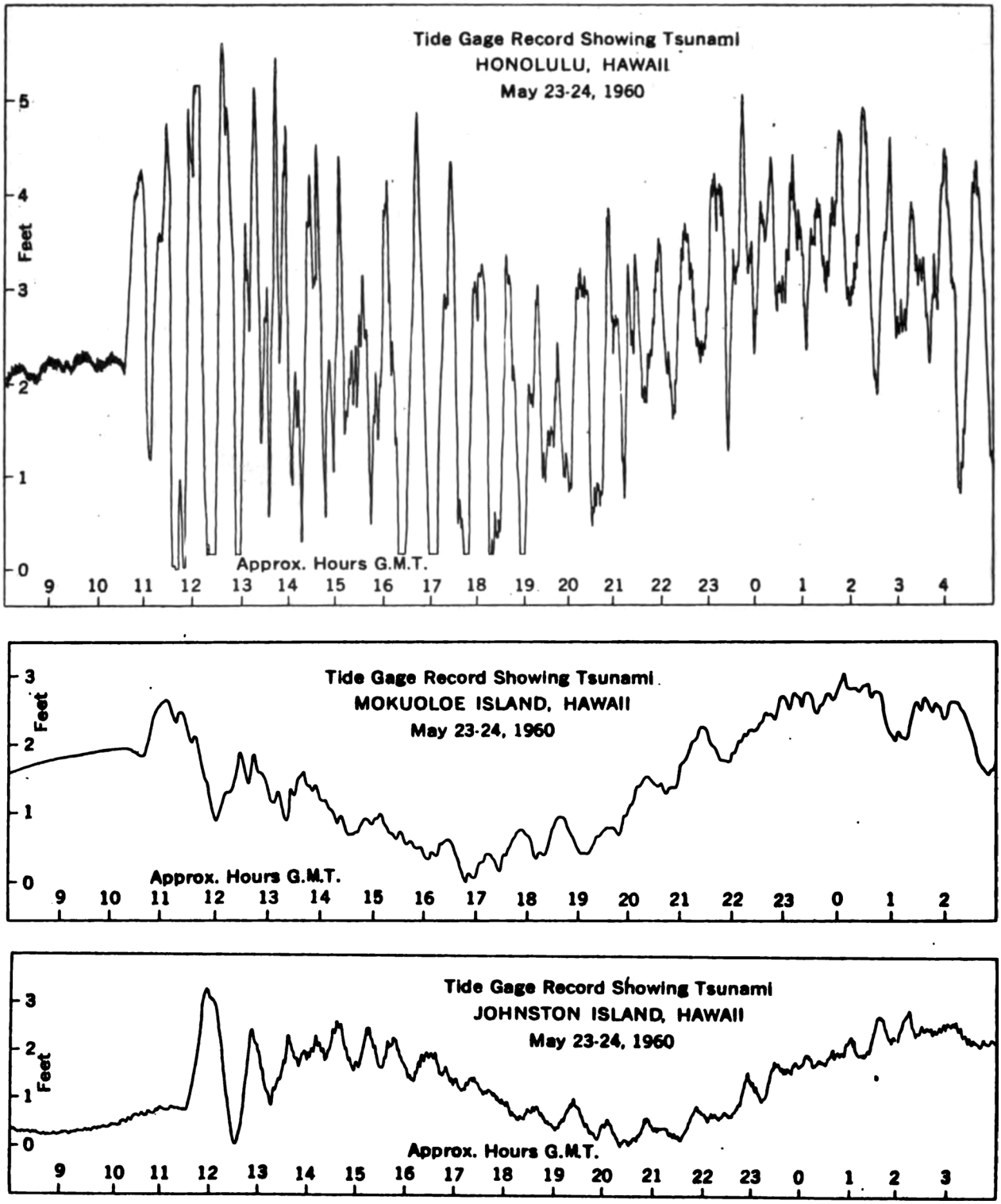

Fig. 1 The 1960 Chile earthquake tsunami recorded at three Pacific Islands (Honolulu, Mokuoloe Island, Johnston Island). Note the precursory phase with negative polarity before the conspicuous tsunami arrival. Copied from Zetler and Symons (1961)

by JMA, four (Kushiro, Hatsushima, DONET1, and Muroto) submarine cables by JAMSTEC, one (Kamaishi) by ERI, and one (Sagami) by NIED were in operation to monitor tsunamis offshore Japan. After the 2011 Tohoku-Oki earthquake, an additional Kamaishi cable by ERI, DONET2 by JMASTEC, and S-net by NIED were installed. Later, the operation of DONET1 and DONET2 was transferred to NIED. Because of technical problems, OBPG installation had been limited to depths of 6000 m or less. S-net is the first submarine cable network for OBPGs to overcome this limitation. OPBGs of modern submarine cable networks, such as S-net, report the absolute water pressure every 0.1 s at the shortest. All S-net cables were laid off the Pacific coast of the Hokkaido and Honshu islands, Japan. The S-net submarine network has one loop east of the Japan Trench. N-net, which covers off the Pacific coast of the Shikoku and Kyushu islands, is being constructed by NIED.

Seabed wave gauges were installed on the seafloor at water depths of 30–50 m to monitor the wave height by measuring the traveltime of acoustic waves between the wave gauge and the sea surface. Analyses of the 2010 Maule (Chile) earthquake tsunami waveforms recorded by a coastal tide gauge, a seabed wave gauge, and an offshore GPS wave gauge along a tsunami raypath to the Japanese coast revealed site- and frequency-dependent amplification factors of tsunami wave components (Kawai et al. 2012).

1.2.3 Deep-sea tsunami records

After the 2004 Sumatra–Andaman earthquake caused a huge and destructive tsunami in the Indian Ocean, NOAA started establishing a basin-wide tsunami observation network for tsunami warnings in the Pacific Ocean by deploying DART tsunamimeters in the deep sea. The BPRs deployed on the deep seafloor at the DART stations continuously record the ocean-bottom pressure, which reflects the surface water level every 15 s. The DART station is battery-powered and operates autonomously. To reduce power consumption, low-sampling rate data every 10 min are transmitted to a surface buoy via acoustic telemetry and then to tsunami warning centers via the GEOSS satellite communication link. The nominal resolution of the water-height data is 1 mm. Because of the large water depth, short-period sea-level changes dominated by swells at the sea surface are effectively filtered out, and thus, the BPR records are only sensitive to long-period components of sea-level changes. A sudden change in pressure triggers a high sampling rate for the telemetry, with an interval of as short as every 15 s. Internally recorded 15-s sampling data are retrieved during the ship operation to replace batteries every one or two years. If the DART BPR is not retrieved, the 15-s sampling data are lost (Meinig et al. 2005).

Ocean-bottom tsunami sensors installed on the offshore seafloor can avoid the complex tsunami wave reflection and refraction from the shallow sloping bathymetric structure and coastal topography. Therefore, assuming that the tsunami propagation Green's function for a sea-surface elevation source is well-established, tsunamis generated, propagated, and recorded in the deep ocean are used to most directly and accurately constrain the tsunami source model and are an ideal dataset for tsunami source inversions (e.g., Satake 2015).

From a retrospective point of view, there were reports of the traveltime delays and initial phase reversals in deep-sea tsunami records of distant tsunamis. A section is quoted from Watada et al. (2014).

> *Rabinovich et al. (2011) noted a 10–15 min delay of the tsunamis that were recorded by two BPRs deployed in the Drake Passage between South America and Antarctica relative to a long-wave simulation after a traveltime of 20 hr from the 2004 Sumatra-Andaman earthquake. The time delays were hypothesized to be related to wave dispersion effects. Wei et al. (2008) and Hébert et al. (2009) showed that a tsunami record at a DART station in the central Pacific Ocean for the 2007 Peru earthquake (M8.0) indicates a 12-15 min delay relative to long-wave simulation after a propagation of 7 hr. The cause of delay was speculated to be inaccurate bathymetry data, source location, and deviation from the linear long-wave assumption. Although not mentioned by the authors, figures presented in these studies, which compare the simulated and observed waveforms, show a clear precursory negative trough before the positive main peak (Figure 3(a) of Wei et al. 2008; Figure 7 of Hébert et al. 2009).*

The tsunami research community's confidence in the traditional distant-tsunami propagation theory was not shaken by these observations until the community was confronted with clear and undeniable observational facts that were inconsistent with theoretical predictions.

2 New studies prompted by trans-Pacific tsunamis recorded at deep oceans

Two new studies have been prompted by the trans-Pacific tsunami recorded at deep ocean following the 2010 Maule (Chile) and 2011 Tohoku-Oki earthquakes. These were the first large interplate earthquakes that occurred near deep ocean trenches and generated trans-oceanic tsunamis after the completion of the DART network

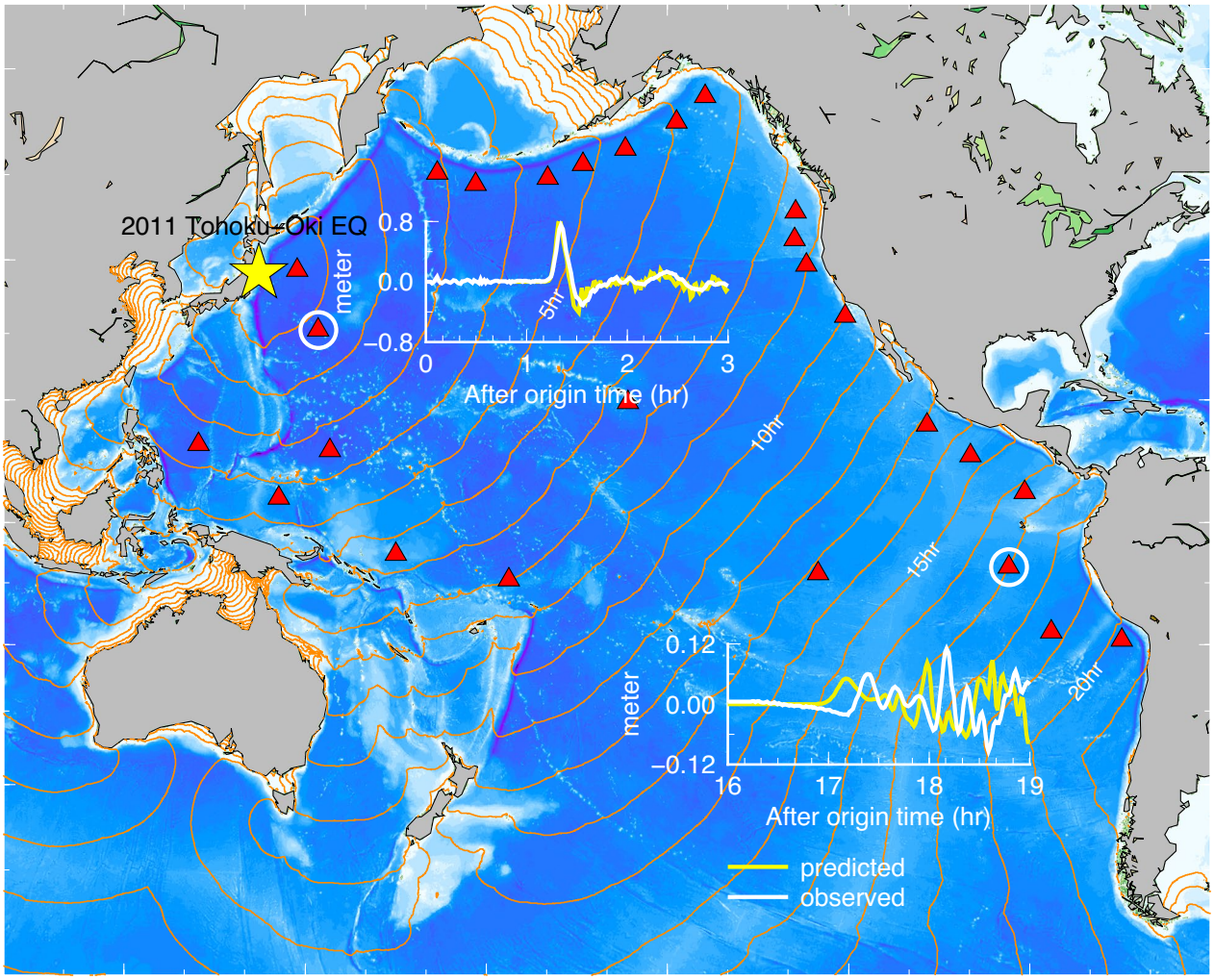

Fig. 2 Traveltime delay and initial phase reversal of the tsunami generated by the 2011 Tohoku-Oki earthquake, denoted by the yellow star. Red triangles indicate the location of DART stations. Observed and conventional synthetic tsunami waveforms are compared at near field (1 h traveltime) and far field (17 h traveltime). Contour lines of the traveltime are drawn at every 1 h. At the near field, the waveforms match well. At the far field, the observed waveform shows a reversed initial phase and traveltime delay relative to the conventional long-wave tsunami simulation

(Fig. 2). About 30 DART stations distributed on the deep Pacific Ocean floor worked as an array and recorded trans-oceanic tsunamis that arrived just a few hours after the earthquake and that nearly one day later reached the opposite shore of the Pacific without interference from shallow coastal structures. In the following sections, we review how these records renew our understanding of trans-oceanic tsunamis and prompt the development of a new tsunami propagation theory.

2.1 Importance of initial phase: an ocean-bottom landslide case

A conventional linear surface gravity wave, whether dispersive or not, preserves the initial motion when the source of the first tsunami is created (Fig. 3b and c), as the phase velocity monotonically increases as the wavelength increases. Tsunami sources are often sea-surface uplift or subsidence caused by large earthquakes, landslides, or volcanic activity in the ocean. The preservation of the initial tsunami motion, regardless of amplitude, is a crucial feature of the tsunami propagation process because it reflects the initial seafloor motion and provides definitive evidence of how the initial seafloor process begins. Seismologists have long studied the minute initial motions of earthquakes of various magnitudes (e.g., Iio 1995) for the same reason, as they preserve the very first process of faulting that radiates seismic waves.

For example, Tappin et al. (2014) argued that the large amplitude tsunami observed along the coast north of the epicenter of the 2011 Tohoku-Oki earthquake

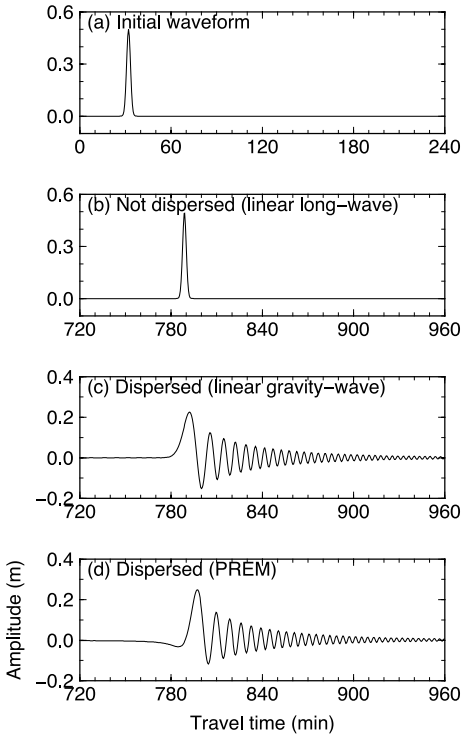

Fig. 3 Dispersive and non-dispersive tsunami propagation simulations for a 4 km deep ocean. **a** An initial Gaussian-shaped tsunami observed at $x=0$ km traveling in the positive x direction, where $u(0,t) = 0.5 * \exp\left(-(t-t_o)^2 * \omega_a^2\right)$ m, $f_a=0.0015$ Hz, $\omega_a = 2\pi f_a$, and $t_o=1920$ s. The time series was computed at every 30 s for 2048 samples, giving a total time length of 1024 min. **b**–**d** Simulated tsunami waveforms at $x=9000$ km that were computed for constant long-wave phase speed, i.e., $\sqrt{gd}$, linear surface gravity wave phase speed in a homogeneous incompressible ocean, i.e., $\omega/k = \sqrt{g(\tanh kd)/k}$, and the phase speed in an ocean coupled with the PREM having a 4 km deep ocean layer, respectively. The arrival times of the peak amplitude in Fig. 3c and d are delayed by 3 min and 8.5 min, respectively, relative to that in Fig. 3b. Note that in Fig. 3d, a small-amplitude initial phase with reversed polarity relative to the main peak precedes the main peak. The figure has been adapted from Fig. 6 of Watada et al. (2014)

was partially caused by a large SMF, an ocean-bottom landslide that occurred on the landward slope of the seafloor near the trench axis north of the epicenter and was induced by seismic ground shaking. A landslide on a landward slope results in an oceanward mass motion that causes initial uplift at the oceanward sea surface and initial subsidence at the landward sea surface (e.g., Fig. 7 of Tappin et al. 2014). Therefore, at coastal observation points, the first motion of a landslide tsunami, regardless of the amplitude, should be downward. In the tsunami waveforms observed at landward stations (e.g., Fig. 2 of Tappin et al. 2014; Fig. 2 of Yamazaki et al. 2011), all initial motions were upward, consistent with the upward motion of the landward upper plate of the shallow low-dip-angle thrust fault of the Tohoku-Oki earthquake. No direct evidence of SMF was found in the first motions of the observed tsunamis. Note that this type of first motion analysis does not preclude the possibility of a later occurrence of the SMF.

2.2 Time domain evidence for delay and initial phase reversal

The first unequivocal evidence for the delayed propagation of trans-oceanic tsunamis was reported for the 2010 Maule (Chile) earthquake tsunami recorded along the coasts of Japan, Canada, and the USA. The DART network captured the initial tsunami waves just a few hours after the earthquake and continuously recorded tsunamis crossing the Pacific and reaching the other side of the basin about 24 h later (e.g., Fig. 4; Fujii and Satake 2013; Watada et al. 2014). As the 2010 Maule (Chile) tsunami crossed the Pacific, multiple and high-quality observations by the DART network provided clear evidence that the existing far-field tsunami theory was inadequate to explain the observed far-field tsunami traveltimes and waveforms. Tsunami sensors attached to the deep ocean-bottom cables recorded tsunamis (Saito et al. 2010), on-land tiltmeters along the Pacific coast of Japan (Kimura et al. 2013), and offshore GPS buoys (Kato et al. 2011) showed delays in tsunami arrivals of up to 30 min relative to linear long-wave simulations. Rabinovich et al. (2013) also noticed a small negative phase with gradual subsidence of the sea level before the sharp increase by the main positive phase in almost all onshore and offshore tsunami records along the Pacific coast of Canada and the USA.

Kawai et al. (2012) examined NOWPHAS GPS wave gauge motion in detail during the 2010 Maule (Chile) tsunami. A GPS wave gauge was installed 10 km off the northeast coast of Honshu, Japan. As the first wave approached, the initial horizontal motion of the GPS wave gauge was eastward, and the vertical motion was downward (Fig. 5). This two-dimensional motion of the GPS wave gauge was consistent with a negative amplitude initial tsunami arriving from the east.

The tsunami research community was puzzled by the tsunami traveltime delay following the 2010 Maule (Chile) earthquake. A few non-tsunami scientists, but seismologists, noticed the inconsistency of the polarity of the initial phases in the far field. Most tsunami scientists, who held a strong belief in the validity of the long-wave propagation theory and placed more emphasis on the peaks than on the initial waves, searched for other explanations, such as errors in the tsunami source location and systematic regional bias in bathymetric data, as well as the effects of alternative numerical schemes,

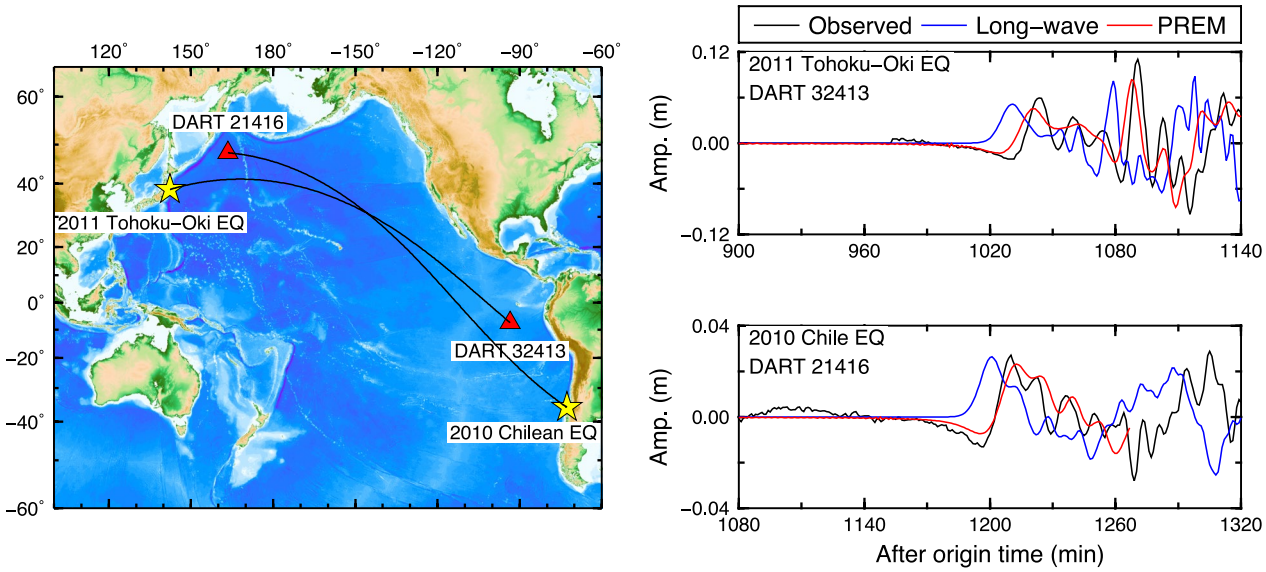

Fig. 4 Trans-Pacific Tsunami waveforms generated by the 2010 Maule (Chile) and 2011 Tohoku-Oki earthquakes. Left) Approximated tsunami raypaths (black lines) from the sources (yellow stars) and DART stations (red triangles). Right) Comparison of the observed (black lines) and two synthetic tsunami waveforms computed by the old (blue lines) and new (red lines) waveform simulation methods. For both earthquakes, the initial phase reversal and traveltime delay of the observed tsunami waveforms are found. With the new waveform synthetic method, the waveform discrepancy diminishes

numerical grid size, and the nonlinear water wave behavior (JMA 2010).

The 2011 Tohoku-Oki earthquake tsunami repeated the same traveltime delays and the initial phase reversals that appeared only in the far field, and changed the minds of tsunami scientists forever. We needed a new tsunami propagation theory to explain the traveltime delay and initial phase reversal. The tsunami research community was still unaware that the two problems were rooted in a common origin.

2.3 Frequency domain evidence for reverse dispersion of tsunamis

The dispersion of surface gravity waves of a homogeneous incompressible inviscid fluid under gravity is expressed as follows:

$$\frac{\omega}{k} = \sqrt{g(\tanh kd)/k} \tag{11}$$

This expression has been used to characterize both non-dispersive long waves and dispersive short waves, and has been confirmed by the observation of distant tsunamis in studies such as Saito et al. (2010). The dispersion relation expressed by Eq. 11 indicates that the wave phase and group speeds become the same $\sqrt{gd}$ at the largest wave period, and the first motion of long waves is conserved at all distances. As observed in Sect. 2.2, the first motions of all distant tsunamis were consistently reversed compared to long-wave simulations. The real tsunami dispersion relation deviates from the conventional dispersion relation expressed in Eq. 11.

Watada et al. (2014) plotted the phase velocities measured from the 2010 Maule (Chile) and 2011 Tohoku-Oki earthquake tsunamis (Fig. 6) recorded by the DART network. All measured phase velocities were normalized to the reference ocean depth, which was $d = 4$ km in this case. At the shortest wave period, the measured dispersion relation is close to the standard dispersion relation expressed in Eq. 11. As the period increases, the phase velocity deviates from the standard dispersion relation, and the phase velocity exhibits a maximum with a value of ~ 1% smaller than the long-wave speed $\sqrt{gd}$ at around 1000 s. Beyond 1000 s, the phase velocity shows reverse dispersion, meaning that the phase speed becomes slower as the period increases. The phase velocity measurements are well explained by the tsunami dispersion curves of the gravitationally coupled elastic Earth (Sects. 2.4 and 2.5). At around 8000 s, the phase velocity is 2% slower than the long-wave speed.

Watada et al. (2014) also confirmed that the reverse dispersion of tsunamis over the longest periods is responsible for the initial phase reversal of distant tsunamis. Figure 3 compares the three tsunamis with specific tsunami dispersion relations. A non-dispersive tsunami that propagates at the same phase speed for all wave period components maintains the wave shape (Fig. 3b).

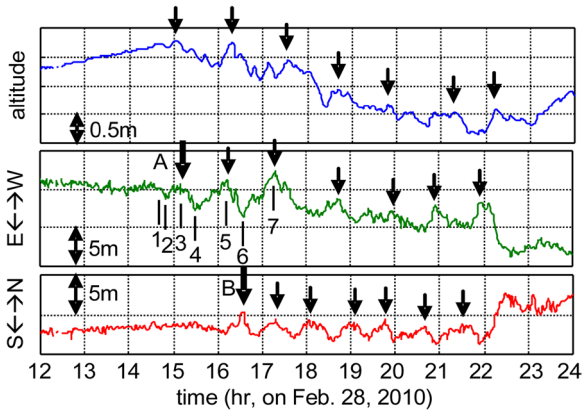

(a) The time series of altitude and longitudinal and latitudinal location

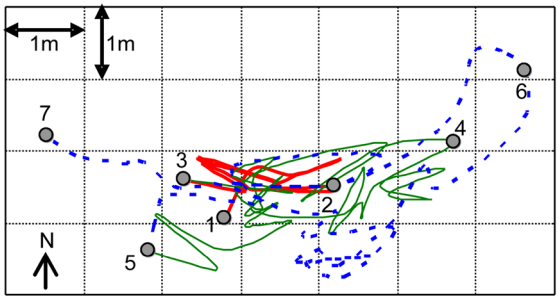

(b) The trace of the horizontal motion caused by the initial part of the tsunami

Fig. 5 Seawater movement revealed by the NOWPHAS GPS wave gauge buoy (#805, Aomori-Togan-Oki) motion installed 10 km off the coast at a water depth of 87 m during the arrival of the 2010 Maule (Chile) earthquake tsunami. The exact location of the GPS wave gauge buoy can be found in Fig. 7a of Kawai et al. (2012). **a** The time series indicate the three dimensional motion of the buoy, which is moored to the seafloor by a chain and is not in completely free motion. **b** The trace of the horizontal motion of the buoy is shown with numbers along the trace corresponding to the timing in the time series in figure (**a**). The first horizontal motion is eastward and the vertical motion is downward from time 1 to time 2. The first vertical and horizontal motions are consistent with a tsunami with a leading negative trough propagating from east to west at the buoy location. The figure has been adapted from Fig. 6 of Kawai et al. (2012)

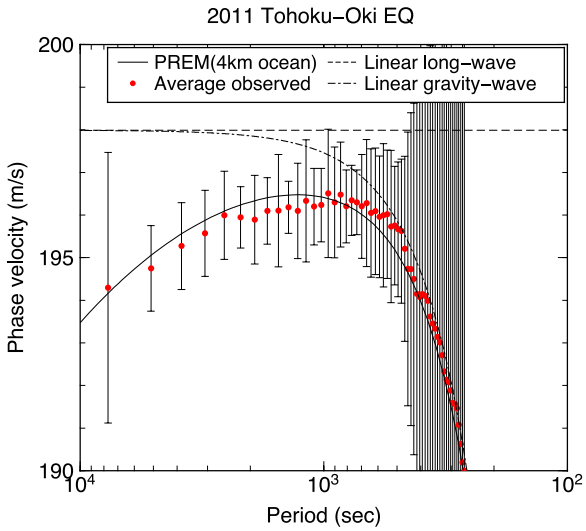

Fig. 6 Comparison of the measured phase velocities (red dots with error bars) and predicted tsunami phase velocities for the 2011 Tohoku-Oki earthquake tsunami. The half of the error bar length at each wave period corresponds to one standard deviation of 25 station measurements. The measured phase velocities fit the predicted tsunami phase velocity of the gravitationally-coupled elastic Earth model, i.e., the PREM model. Two other theoretical tsunami phase velocity models are plotted. The dashed line represents a non-dispersive constant long-wave tsunami speed given by $\omega/k = \sqrt{gd}$, where $g = 9.822$ m/s^2 and $d = 4$ km. The dash-dotted line expresses the linear surface gravity wave given by $\omega/k = \sqrt{g(\tanh kd)/k}$. The figure has been adapted and modified from Fig. 9 of Watada et al. (2014)

The dispersive linear gravity waves that propagate at the speed described by Eq. 11 are dispersive, and the initial upward motion remains unchanged (Fig. 3c). A tsunami that propagates at a phase speed with reverse dispersion at the longest periods shows a reversed initial phase (Fig. 3d).

2.4 Physics of gravitationally coupled elastic Earth system

The governing equations and boundary conditions for the deformation problem of a spherically symmetric gravitationally coupled elastic Earth (e.g., Alterman et al. 1959; Takeuchi and Saito 1972; Watada and Kanamori 2010) are introduced. The Earth model is composed of elastic layers corresponding to the crust, mantle, and inner core, and fluid layers corresponding to the ocean and outer core. The density and elastic parameters of the fluid and solid layers can be a function of radius.

2.4.1 *Tsunami as a wave in a gravitationally coupled elastic Earth system*

The linear momentum equation is:

$$\rho \frac{d\boldsymbol{v}}{dt} \equiv \rho \left(\frac{\partial \boldsymbol{v}}{\partial t} + (\boldsymbol{v} \cdot \nabla)\boldsymbol{v} \right) = \nabla \cdot \boldsymbol{\tau} + \rho \boldsymbol{g} \tag{12}$$

where $\rho, \boldsymbol{g}, \boldsymbol{v}, \boldsymbol{u}, \boldsymbol{\tau}$ are the density, gravity vector, velocity vector, displacement vector, and stress tensor, respectively. All quantities are defined as a function of the fixed position $\boldsymbol{x}$ and time t. Here, we consider the small deformation of the Earth, where the second order of displacement is ignored, and the deformation process is adiabatic, i.e., we ignore the heat conduction and radiation processes. There are two ways to describe a small change in quantity $f(\boldsymbol{x}, t)$ by small deformation $\boldsymbol{u}$. The change measured at a fixed position $\boldsymbol{x}$ is the Eulerian

perturbation, denoted by $f'(\boldsymbol{x},t)$. The change measured at the point moving with the deforming medium $\boldsymbol{x}=\boldsymbol{x}_o+\boldsymbol{u}$ is the Lagrangian perturbation denoted by $\delta f(\boldsymbol{x},t)$, where $\boldsymbol{x}_o$ is the initial position before deformation. Hereafter, $f_o(\boldsymbol{x})$ represents quantity f at $\boldsymbol{x}$ before deformation.

$$f(\boldsymbol{x},t)=f_o(\boldsymbol{x}_o)+\delta f(\boldsymbol{x},t) \tag{13}$$

$$f(\boldsymbol{x},t)=f_o(\boldsymbol{x})+f'(\boldsymbol{x},t) \tag{14}$$

Note that the Lagrangian and Eulerian perturbations differ to the first order of $\boldsymbol{u}$

$$\delta f(\boldsymbol{x},t)=f^{'}(\boldsymbol{x},t)+\boldsymbol{u}\cdot\nabla f_o(\boldsymbol{x}) \tag{15}$$

but are convertible if we know $\boldsymbol{u}$ and $f_o(\boldsymbol{x})$. For example, the Eulerian density perturbation is expressed as:

$$\rho^{'}=-\nabla\cdot(\boldsymbol{u}\rho) \tag{16}$$

The Lagrangian density perturbation is expressed as:

$$\delta\rho=-\rho(\nabla\cdot\boldsymbol{u}) \tag{17}$$

The two density perturbations differ to the first order of $\boldsymbol{u}$

$$\delta\rho(\boldsymbol{x},t)=\rho'(\boldsymbol{x},t)+\boldsymbol{u}\cdot\nabla\rho_o(\boldsymbol{x}) \tag{18}$$

The equilibrium initial state means:

$$\nabla\cdot\boldsymbol{\tau}_o+\rho_o\boldsymbol{g}_o=0 \tag{19}$$

We assume that the Earth's initial stress $\boldsymbol{\tau}_o$ is isotropic and under hydrostatic equilibrium, i.e.,

$$\boldsymbol{\tau}_o(\boldsymbol{x})=-p_o(\boldsymbol{x})\boldsymbol{I} \tag{20}$$

where p_o is the initial hydrostatic pressure, and $\boldsymbol{I}$ is the unit tensor. $\boldsymbol{g}_o$ is the time-constant gravity vector under the initial equilibrium but can vary in space. Therefore, we have:

$$\nabla p_0(\boldsymbol{x})=\rho_o(\boldsymbol{x})\boldsymbol{g}_o(\boldsymbol{x}) \tag{21}$$

where $\boldsymbol{x}=(r,\theta,\phi)$. r,θ,ϕ are the radial, colatitudinal, and longitudinal coordinates, respectively, in a spherical coordinate system. The scalar gravity value g_o is defined by $\boldsymbol{g}_o(\boldsymbol{x})=(-g_o(r),0,0)$, and we obtain a familiar formula for the hydrostatic pressure gradient balanced by gravity:

$$\frac{dp_o(r)}{dr}=-\rho_o(r)g_o(r) \tag{22}$$

By subtracting Eq. 21 from Eq. 12 and keeping only the first-order perturbations and first-order of displacement, we obtain the linearized equation of motion for perturbed states in a fluid:

$$\rho_o\frac{\partial^2\boldsymbol{u}}{\partial t^2}=-\nabla p'+\rho^{'}\boldsymbol{g}_o+\rho_o\boldsymbol{g}' \tag{23}$$

and in a solid:

$$\rho_o\frac{\partial^2\boldsymbol{u}}{\partial t^2}=\nabla\cdot\boldsymbol{\tau}^{'}+\rho^{'}\boldsymbol{g}_o+\rho_o\boldsymbol{g}' \tag{24}$$

where we have used $\boldsymbol{v}=\frac{d\boldsymbol{u}}{dt}=\frac{\partial\boldsymbol{u}}{\partial t}+(\boldsymbol{v}\cdot\nabla)\boldsymbol{u}=\partial\boldsymbol{u}/\partial t$ to the first order of $\boldsymbol{u}$. The Eulerian density perturbation is written as:

$$\rho^{'}(\boldsymbol{x},t)=\delta\rho(\boldsymbol{x},t)-\boldsymbol{u}(\boldsymbol{x},t)\cdot\nabla\rho_o(\boldsymbol{x}) \tag{25}$$

The Eulerian pressure perturbation is written as:

$$\begin{aligned}p^{'}(\boldsymbol{x},t)&=\delta p(\boldsymbol{x},t)-\boldsymbol{u}(\boldsymbol{x},t)\cdot\nabla p_o(\boldsymbol{x})\\&=\delta p(\boldsymbol{x},t)+u_r(\boldsymbol{x},t)\rho_o(r)g_o(r)\end{aligned} \tag{26}$$

where $\boldsymbol{u}=(u_r,u_\theta,u_\phi)$ in the spherical coordinate system.

Constitutive equations are derived from the properties of the medium, and thus, the Lagrangian stress change or pressure change is used to describe them. The constitutive equation for the adiabatic compression of a fluid is defined by the density and volume perturbations:

$$\delta p(\boldsymbol{x},t)=c_s^2\delta\rho(\boldsymbol{x},t)=\frac{K(\boldsymbol{x})}{\rho_o(r)}\delta\rho(\boldsymbol{x},t)=-K(\boldsymbol{x})\nabla\cdot\boldsymbol{u}(\boldsymbol{x},t) \tag{27}$$

where c_s is the sound velocity of the fluid, and K is the bulk modulus of the medium.

The constitutive equation for a solid under adiabatic deformation is a generalized Hook's law with elastic constants. For an isotropic elastic body, the constitutive equation is given by:

$$\delta\boldsymbol{\tau}=\left(K-\frac{2}{3}\mu\right)(\nabla\cdot\boldsymbol{u})\boldsymbol{I}+2\mu\boldsymbol{e} \tag{28}$$

where μ is the rigidity of the medium, and $\boldsymbol{e}$ is a strain tensor caused by displacement $\boldsymbol{u}$. $\boldsymbol{u}$ itself is a small quantity of the first order, and the difference between the Eulerian and Lagrangian forms is neglected. Similarly, $\boldsymbol{e}$ is a linear function of $\boldsymbol{u}$ and the difference between the two forms is neglected. The Eulerian stress perturbation is written as:

$$\begin{aligned}\boldsymbol{\tau}^{'}(\boldsymbol{x},t)&=\delta\boldsymbol{\tau}(\boldsymbol{x},t)-\boldsymbol{u}(\boldsymbol{x},t)\cdot\nabla\boldsymbol{\tau}_o(\boldsymbol{x})\\&=\delta\boldsymbol{\tau}(\boldsymbol{x},t)-u_r(\boldsymbol{x},t)\rho_0(r)g_0(r)\boldsymbol{I}\end{aligned} \tag{29}$$

and is used in Eq. 24.

We have a Poisson's equation for the gravitational potential ϕ defined by gravity $\boldsymbol{g}$ and the density distribution ρ:

$$\nabla^2\phi = -\nabla\cdot\boldsymbol{g} = 4\pi G\rho \tag{30}$$

Using $\nabla\phi_0 = \boldsymbol{g}_0, \nabla\phi' = \boldsymbol{g}'$, the initial gravitational potential and the Eulerian perturbation of the gravitational potential are described as:

$$\nabla^2\phi_0(\boldsymbol{x}) = -\nabla\cdot\boldsymbol{g}_0(r) = \frac{dg_0(r)}{dr} + \frac{2}{r}g_0(r) = 4\pi G\rho_0(r) \tag{31}$$

$$\nabla^2\phi'(\boldsymbol{x},t) = -\nabla\cdot\boldsymbol{g}'(\boldsymbol{x},t) = 4\pi G\rho'(\boldsymbol{x},t) = -4\pi G\nabla\cdot(\boldsymbol{u}(\boldsymbol{x},t)\rho_0(r)) \tag{32}$$

Then, the linearized equation of motion (Eq. 24) is written as:

$$\begin{aligned}\rho_o\frac{\partial^2\boldsymbol{u}}{\partial t^2} &= \nabla\cdot\boldsymbol{\tau}' + \rho'\boldsymbol{g}_o + \rho_o\boldsymbol{g}' \\ &= \nabla\cdot\delta\boldsymbol{\tau}(\boldsymbol{x},t) - \nabla\big(u_r(\boldsymbol{x},t)\rho_0(r)g_o(r)\big) \\ &\quad + g_0(r)\nabla\cdot(\boldsymbol{u}(\boldsymbol{x},t)\rho_o(r))\hat{\boldsymbol{r}} \\ &\quad + \rho_o(r)\nabla\phi'(\boldsymbol{x},t)\end{aligned} \tag{33}$$

where $\hat{\boldsymbol{r}}$ is the unit vector in the radial direction. The first term represents the elastic force caused by deformation. The third and fourth terms represent the gravitational forces due to the change in density and the change in gravity, respectively. The second term is often neglected but is required when we use the Lagrangian stress caused by strain (Eq. 28).

For a fluid, the linearized equation of motion is written as:

$$\begin{aligned}\rho_o\frac{\partial^2\boldsymbol{u}}{\partial t^2} &= -\nabla\delta p(\boldsymbol{x},t) - \nabla\big(u_r(\boldsymbol{x},t)\rho_o(r)g_o(r)\big) \\ &\quad + g_0(r)\nabla\cdot(\boldsymbol{u}\rho_o(r))\hat{\boldsymbol{r}} + \rho_o(r)\nabla\phi'(\boldsymbol{x},t)\end{aligned} \tag{34}$$

In geophysical fluid mechanics, the Earth's gravity is often assumed to be a time constant, and the last term is neglected. We retain all terms in the following.

At the fluid–fluid and fluid–solid interfaces, δp and u_r are continuous, and at the solid–solid interface, $\delta\boldsymbol{\tau}$ and $\boldsymbol{u}$ are continuous. At any types of interface, $\hat{\boldsymbol{r}}\cdot(\nabla\phi' + 4\pi G\rho_0(r)\boldsymbol{u})$ is continuous. For free oscillation problems, the surface boundary condition for a fluid requires zero pressure, i.e., $\delta p = 0$, and for a solid, it requires vanishing surface traction, i.e., $\hat{\boldsymbol{r}}\cdot\delta\boldsymbol{\tau} = 0$. For both solid and fluid cases $\hat{\boldsymbol{r}}\cdot\left(\nabla\phi' + 4\pi G\rho_0(r)\boldsymbol{u}\right) = 0$ is required as an additional surface boundary condition described by the gradient of the gravitational potential perturbation and the displacement. For forced oscillation problems caused by an external periodic surface mass load, the surface boundary conditions should be set to match the external sources using the combinations of displacement, traction, gravitational potential, or gradient of gravitational potential, e.g., Farrell (1972).

2.4.2 Eulerian variables and Lagrangian variables

In fluid mechanics, which includes meteorology, oceanography, and helioseismology, pressure perturbation is customarily an Eulerian variable. The Eulerian pressure perturbation does not vanish at the grid point that is initially on the water surface under gravity (e.g., Dingemans 1997a). Here, the Eulerian pressure perturbation can be converted using Eq. 15 into the Lagrangian pressure perturbation of a moving grid point, which has been customarily used in solid mechanics including solid material science and seismology. At an internal boundary with a density jump, the Eulerian pressure or Eulerian traction normal to the internal boundary has a jump in pressure or traction by $(\rho_a - \rho_b)g(r_o)u_r$, where ρ_a and ρ_b are densities above and below the boundary at r_o, respectively.

In both free oscillation and forced oscillation problems, the differential equations that describe the vibration of a system with appropriate surface boundary conditions are solved in the frequency domain using global bases that span the entire system. The time-derivative terms are replaced by frequency multiplication. The equation of motion (Eq. 33 or Eq. 34) represents three first-order homogeneous simultaneous linear differential equations (HSLDEs) with respect to radius. Poisson's equation for the gravitational potential perturbation (Eq. 32) represents a second-order HSLDE. The constitutive equation for a fluid (Eq. 27) indicates that the pressure perturbation in Eq. 34 is converted into the first-order spatial derivatives of the displacements. Likewise, the constitutive equation for a solid (Eq. 28) indicates that the stress perturbation in Eq. 33 is converted into first-order spatial derivatives of the displacements. For either a fluid or a solid, we have four second-order HSLDEs in total for four unknown variables $\boldsymbol{u}, \phi'$ after eliminating the pressure and stress perturbations.

The differential equations and the boundary conditions expressed in Eulerian variables, Lagrangian variables, or mixed variables (e.g., Eq. 33 contains the Lagrangian variable $\delta\boldsymbol{\tau}$ and Eulerian variable ϕ') for small oscillation problems might look different. However, the equations and boundary conditions are entirely compatible through the conversion of the dependent variables using Eq. 15. The eigenfrequency solutions of the free oscillation problem are unchanged, irrespective of the choice of the type of variables. Therefore, the dispersion relation that characterizes the relationship between the wavelength and wave period of modal solutions is always the same. The

eigenfunction solutions of the displacement variables are also the same, irrespective of the choice of variable type. The eigenfunction solutions of the pressure or stress variables appear different depending on the Lagrangian or Eulerian type variables, but they are convertible to each other using Eq. 15.

2.4.3 Tsunami as a free-oscillation of the Earth system

In the first approach, a tsunami, as with a seismic wave, is a free wave of the gravitationally coupled elastic Earth. To solve the free oscillation problems of the Earth, Alterman et al. (1959) reformulated each second-order differential equation (Sect. 2.4.2) into two simultaneous first-order differential equations by adopting the stress-traction components and radial gradient of gravitational potential as intermediate variables. They demonstrated in a solid that, due to spherical symmetry, first-order HSLDEs for eight unknowns (four original and four intermediate variables) can be separated into first-order HSLDEs for six unknowns that govern the spheroidal motions and first-order HSLDEs for two unknowns that govern the toroidal motions. Detailed steps of reformulating the second-order differential equations into first-order HSLDEs for four unknowns that govern the spheroidal motions in a self-gravitating fluid are given, for example, in Appendix A of Watada and Kanamori (2010).

A tsunami mode of a gravitationally coupled elastic Earth is composed of a pair of an eigenfrequency and eigenfunctions defined in both the ocean and solid Earth layers. The eigenfunctions in the ocean represent the water wave motion, and those in the solid Earth represent the deformation in the solid Earth at the eigenfrequency. Ward (1980) and Okal (1982) numerically solved the HSLDEs and free surface boundary conditions for eigenfrequencies and eigenfunctions of a spherically symmetric Earth with a surface ocean layer, and Watada and Kanamori (2010) solved the HSLDEs for a spherically symmetric Earth with a surface ocean layer and an atmospheric layer. The obtained tsunami mode eigenfrequency solutions were then used to construct a tsunami dispersion curve that describes the tsunami propagation speed as a function of the wave period in the gravitationally coupled elastic Earth. The tsunami dispersion curve is used in the phase correction method (Sect. 2.6.1).

2.4.4 Tsunami as a surface excess loading mass on the Earth system

In the second approach, seawater is an extra fluid material that imposes variable surface loads and additional surface gravitational potentials as the water waves travel on the exterior surface of the gravitationally coupled elastic Earth at the speed of $\sqrt{gd}$. To solve the surface deformation problems of the Earth caused by periodic surface loads, Farrell (1972) used the same HSLDE part of a free oscillation of the Earth (Sect. 2.4.3) but with an inhomogeneous surface boundary condition expressing a forced oscillation with fixed ω_o at the frequency of the semidiurnal tide. In terms of the surface boundary conditions, a surface point mass load acts in two ways: first, as a periodic force applied to a surface point, and second, as an external gravitational potential caused by the point mass. Responding to the applied gravitational potential, the Earth deforms and generates an additional gravitational potential. The surface boundary conditions of the forced oscillation by a surface point mass are the surface traction equivalent to the point force and the gravitational potential as the sum of the gravitational potential by the surface point mass and the additional gravitational potential caused by the deformed Earth. The surface boundary conditions for the geoid (i.e., the perturbation of the gravitational potential) and the seafloor deformations as the Earth's response to a point mass load on the surface are described by the load Love numbers (Farrell

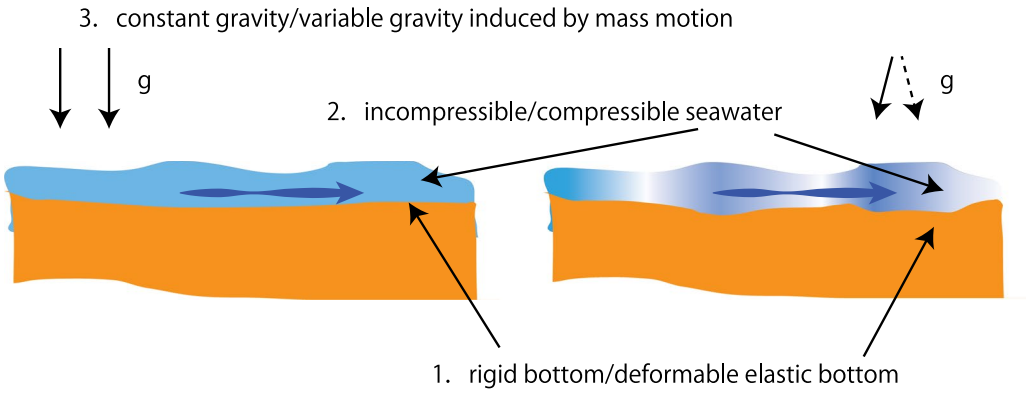

Fig. 7 A cartoon showing the three effects considered in the new tsunami propagation theory: 1. elasticity of the Earth; 2. compressibility of seawater; and 3. spatiotemporal variations in the gravity field

1972). The deformation of the Earth described by the load Love numbers has been extensively used in ocean tide theory.

After setting up first-order SLDEs for six unknowns with appropriate boundary conditions describing a periodic point mass loading for a spherically symmetric Earth without a surface ocean layer, we numerically solve them and obtain the $\boldsymbol{u}$ and ϕ' solutions. The displacement and gravitational potential solutions for a point surface mass loading are the two Green's functions used to calculate the seafloor deformation and the gravitational potential change due to seawater loading during the propagation of tsunamis on the exterior of the Earth system (Sect. 2.6.3).

2.5 Various effects on tsunamis of a gravitationally coupled elastic Earth

In this section, following Watada et al. (2014), we explain the three effects that slow down tsunami speed and the initial phase reversal of distant tsunamis (Fig. 7).

2.5.1 Compressibility and density stratification of seawater

The normal mode theory of tsunamis assumes that waves are linear waves, i.e., small amplitude oscillations, and that Earth materials, including seawater, deform adiabatically. However, the theory does not assume that the horizontal wavelength is larger than the ocean depth. Therefore, the normal mode theory of water waves covers both long- and the short-wave dispersions for a gravitationally coupled elastic Earth system. To examine the effect of seawater compressibility on the tsunami propagation speed, we compared the dispersion relations of water waves for two Earth models. One Earth model is the anisotropic PREM proposed by Dziewonski and Anderson (1981). We modified the depth of the original PREM, which has a 3 km deep ocean to 4 km by replacing the top crust layers with seawater. The anisotropic PREM is described by a density, as well as five elastic constants that describe azimuthally-isotropic anisotropy, often simply called radial anisotropy, as functions of radius. The ocean is constant-density seawater, which is gravitationally unstable (Sect. 1.1.1). The other model has the same 4 km deep ocean, but the seawater is homogeneous incompressible, which is approximated by a very high compressional velocity. Figure 8 shows the dispersion curves of the two Earth models. The black and blue solid lines represent the PREM and the PREM with incompressible seawater dispersion curves, respectively (Fig. 8a). The difference between the two curves is shown in Fig. 8b. The period-independent constant phase velocity reduction (Sect. 1.1.1) exists only for long waves. Okal (1982) estimated the speed reduction ratio for homogeneous compressible water as $gd/6c_s^2$ where c_s is the sound velocity in

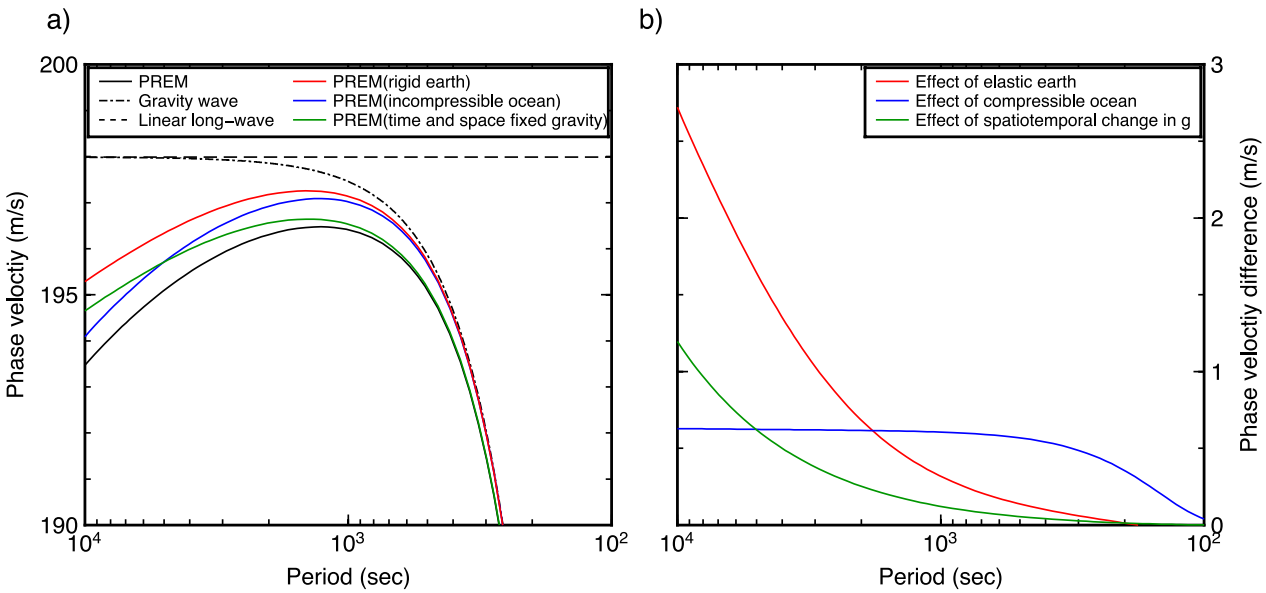

Fig. 8 Period dependency of the three effects considered in the new tsunami propagation theory. **a** Dispersion relations of the tsunami phase velocity computed for various spherical Earth models, all with an ocean layer with $d = 4$ km. The dashed line represents a non-dispersive constant long-wave tsunami speed given by $\omega/k = \sqrt{gd}$, where $g = 9.822$ m/s^2. The dash-dotted line expresses the linear surface gravity wave given by $\omega/k = \sqrt{g(\tanh kd)/k}$. The black line was computed for the anisotropic PREM with a 4 km deep ocean layer, not for an isotropic PREM. The blue, green, and red lines were computed for the modified PREM models; see Watada and Kanamori (2010) for the details of each modification. All normal modes were computed with the physical dispersion defined in the PREM model. **b** Difference of the three modified PREM phase velocities relative to the RREM with a 4 km deep ocean. The figure has been adapted and modified from Fig. 5 of Watada et al. (2014)

the water layer (See Eq. 7). At short periods of less than 2000 s, the compressibility effect has the largest impact on tsunami speed among the three effects. The density stratification further reduces the tsunami speed, and the reduction ratio will be $gd/4c_s^2$ for adiabatically stratified water layer (Tsai et al. 2013; Watada 2013) (See Eq. 8). Watada et al. (2014) explained the period-independent seawater compressibility effect on tsunami propagation speed by introducing self-similarity in the seawater motion of tsunamis. The difference in the water waves between compressible and incompressible seawater diminishes to zero as the waves become short waves (Fig. 8b).

2.5.2 Gravitational attraction due to mass redistribution by moving seawater and deformation of the Earth

The effect of gravitational potential change on the speed of tsunami propagation can be measured by comparing two dispersion curves of two distinct governing equations of motion of the Earth. One curve is obtained using the normal mode method for the PREM (Sect. 2.4.3), while the other is obtained for the same PREM using the normal mode method but without the gravitational potential perturbation, i.e., the gravity is time constant, and $\boldsymbol{g}'$ and ϕ' are zero in Eqs. 33 and 34. The normal mode computation without the gravitational potential perturbation, but with the time-constant reference gravitational potential, is conceptually equivalent to the conventional tsunami computation in which Earth's gravity is time constant. This approximation for the gravitational potential perturbation is called the Cowling approximation (Cowling 1941) and is used for the normal modes of the Earth and stars in cases where the gravitational potential perturbation is unimportant, but gravity plays an essential role in the modes. In Fig. 8a, the green line represents the dispersion curve for the PREM under the Cowling approximation. The difference between the curves with and without the Cowling approximation is plotted in Fig. 8b. The effect of the gravitational potential perturbation is negligible for tsunamis with periods less than 1000 s, but increases as the period increases and becomes the second-largest effect after the elastic Earth effect at periods greater than 5000 s. The effect of the gravitational potential perturbation on the tsunami phase velocity is strongly period-dependent and reduces the tsunami speed as the period increases. In other words, the gravitational potential perturbation contributes to the reverse dispersion of a tsunami.

2.5.3 Elasticity of deformable Earth

The elasticity effect of the solid Earth is already roughly estimated by assuming that the seafloor is a homogeneous elastic half-space (Sect. 1.1.2). Here, we estimate the effect of the elastic solid Earth on the propagation speed of a tsunami more precisely. We assume that the PREM dispersion curve (black solid line in Fig. 8a) is obtained from the linear surface gravity wave dispersion (dash-dot line in Fig. 8a) by subtracting the sum of the three effects, including seawater compressibility, solid Earth elasticity, and gravity potential perturbation. Since we have already evaluated the seawater compressibility and gravitational perturbation effects on the phase velocity (Sects. 2.5.1 and 2.5.2), the remaining effect should come from the solid Earth elasticity. The tsunami phase velocity reduction due to the solid Earth elasticity is shown as the red line in Fig. 8b, and the tsunami propagation speed for a rigid seafloor model is plotted as the red line in Fig. 8a. The elasticity of the solid Earth has the largest effect at the periods longer than 2000 s and reduces the tsunami speed as the period increases. In other words the elasticity of the solid Earth also contributes to the reverse dispersion of a tsunami.

2.6 Synthetic methods

In this section, we introduce two methods for the synthesizing of a realistic tsunami that includes all the effects discussed in Sect. 2.5: The first is the phase correction method developed by Watada et al. (2014), and the second is the convolution method of ocean loading Green's functions developed by Allgeyer and Cummins (2014). Both methods are derived from the same set of governing differential equations, e.g., Alterman et al. (1959), for different Earth models and with different boundary conditions. The resulting waveforms are virtually the same (see Fig. 4 of Kusumoto et al. 2020). However, the realization techniques mostly differ because the former treats the tsunami as a free wave in the Earth system (Sect. 2.4.3), and the latter as an external deformation source of the Earth system (Sect. 2.4.4), contrasting the advantages and disadvantages of the two methods.

2.6.1 Phase correction method

A continuous tsunami dispersion relation $c(\omega)$, which determines the phase speed of a tsunami as a function of the wave period, is obtained from the discrete the normal mode eigenfrequency solutions as $c(\omega_l) = \frac{\omega_l}{k} = \frac{\omega_l a}{\sqrt{l(l+1)}}$ by interpolation, where ω_l is the eigenfrequency of the tsunami mode, l is the angular order of the tsunami mode and an integer. The period-dependent tsunami phase velocity computed from the normal mode solutions precisely predicts the change in tsunami waveforms including all the effects discussed in Sect. 2.5, for a spherically symmetric Earth model. However it cannot be used directly to compute tsunamis in the real Earth. Large bathymetric variations in shallow and deep oceans significantly change the tsunami propagation speed.

Thinking of two tsunamis propagating in the identical bathymetric terrain, one is a conventional non-dispersive tsunami propagating over the rigid seafloor in incompressible seawater, and the other is a realistic dispersive tsunami propagating over the gravitationally-coupled elastic seafloor in compressible seawater; Watada et al. (2014) found that in the frequency domain, irrespective of the bathymetric topography, the phase difference between the two tsunamis is expressed by using a phase velocity difference normalized to a reference ocean depth (Eq. 36). Based on this simple relationship between the phase difference and the phase velocity difference of the two tsunamis, Watada et al. (2014) developed a quick and precise synthetic waveform computation method for tsunamis of a gravitationally coupled elastic Earth system with real bathymetric topography by applying a frequency-dependent phase correction to conventional long-wave tsunami simulations (Eq. 37). This method is explained using the following equations:

We prepare a long-wave tsunami simulation waveform $u(x,t)$ at distance x and time t.

$$u(x,t) = \frac{1}{\pi}\int_0^\infty \widehat{u}(x,\omega)\cos(\Psi(x,\omega))d\omega \tag{35}$$

From the waveform time series, we compute the amplitude spectrum $\widehat{u}(x,\omega)$ and the phase spectrum $\Psi(x,\omega)$ by FFT. The phase correction term is computed as follows:

$$\Delta\Psi(x,\omega) = \int_{raypath} \frac{\Delta c(x,\omega)\omega}{gd(x)}dx = \frac{\Delta c_o(\omega)\omega}{gD_o}L \tag{36}$$

where $d(x)$ and $c(x,\omega)$ are the ocean depth and the phase velocity at x along the tsunami raypath, $\Delta c(x,\omega) = \sqrt{gd(x)} - c(x,\omega)$ is the tsunami phase velocity reduction from the long-wave speed, D_o and $c_o(\omega)$ are the reference ocean depth and the phase velocity of the PREM tsunami propagating in an ocean of depth D_o, $c_o(\omega)$ corresponds to the solid back line in Fig. 8a, $\Delta c_o(\omega) = \sqrt{gD_o} - c_o(\omega)$ is the tsunami phase velocity reduction normalized to the reference ocean depth, and $L = \int_{raypath} dx$ is the tsunami raypath length between the tsunami source and the observation point approximated by the along great circle path. Note that the second identity in Eq. 36 is a unique characteristic of long waves discovered by Watada et al. (2014), which indicates that the phase change of a tsunami propagating over a real terrain along the raypath is replaced by the phase change of a tsunami propagating over an ocean with a reference depth. The reference ocean depth can be any depth we choose. The use of the constant ocean depth eliminates the numerically heavy integral in the first identity. Then, the phase-corrected waveform is computed by IFFT.

$$u(x,t) = \frac{1}{\pi}\int_0^\infty \widehat{u}(x,\omega)\cos(\Psi(x,\omega) + \Delta\Psi(x,\omega))d\omega \tag{37}$$

The phase-corrected waveform is the tsunami waveform of a gravitationally-coupled elastic Earth system. The computation time of the forward FFT (Eq. 35) and the backward IFFT (Eq. 37) is a small fraction of a second and is completely negligible compared to the long-wave simulation time. This is a great advantage of the phase correction method because the total computation time of the tsunami waveforms of a gravitationally-coupled elastic Earth system is almost the same as the conventional long-wave computation time. We can use any conventional long-wave simulation code to compute long waves and apply a phase correction to them.

Ho et al. (2017) replaced the original homogeneous seawater layer of the PREM with an adiabatically density-stratified layer, which reduces the long-wave speed (Sect. 2.5.1). They also computed the tsunami raypath length by searching for the minimum tsunami traveltime raypath from the source to the station, while Watada et al. (2014) approximated the tsunami raypath as a great circle path. These two improvements in the phase correction method change the tsunami traveltime, but do not change the tsunami waveforms. Finally, they strictly follow the integral in Eq. 36 along the raypath instead of using the reference depth, which greatly simplified the computation of the phase correction $\Delta\Psi$ in Watada et al. (2014). These improvements reduced the traveltime difference between the observed and simulated tsunamis but little changed the simulated waveforms. For far-field tsunami stations, adopting approximated great-circle path length changes the path length by less than 10% of the total path length (see Table 2 of Ho et al. (2017)). Therefore, the approximated great-circle path length is used unless we discuss the traveltime within an accuracy of 1–2 min of trans-oceanic tsunamis.

The phase correction method assumes that the tsunami propagation distance $L = \int_{raypath} dx$ from a source to a station does not change. In a single tsunami trace, the leading part is the direct wave from the source, but the later parts contain reflected waves that have traveled a distance greater than L, i.e., not the minimum traveltime raypath. The later part of the phase-corrected tsunami waveform becomes less accurate after long propagation.

2.6.2 *Extension to dispersive surface waves*

The phase correction method, as described in the previous section, was developed for non-dispersive long

waves using long waves as a reference for dispersion. Deviations of the real Earth dispersion from the reference dispersion are assumed to be small, and second-order terms are neglected. Recently developed tsunami observation systems allow for a sampling rate of 1 s or less (Sect. 1.2). Tsunami observations in deep oceans show wave dispersion at periods below 1000 s (e.g., Saito et al. 2010), requiring waveform modeling down to 100 s or less. Sandanbata et al. (2021) extended the phase correction method for dispersive short waves down to a period of ~ 40 s by evaluating the phase correction without assuming it to be small. At these short periods and in the deep oceans, the standard Boussinesq-type approximated dispersion relation becomes highly inaccurate and cannot be used as a reference dispersion. This is because, even after the first- and second-order corrections to the Boussinesq-type dispersion, the phase-corrected dispersion relation is still far from the real dispersion expressed by Eq. 11. Instead, the period-dependent linear surface gravity wave dispersion expressed by Eq. 11 was used as a reference dispersion for short-period tsunamis. Sandanbata et al. (2021) found that the effects of density-stratified compressible seawater and the elasticity of the solid Earth are needed to explain the observed dispersive tsunamis recorded at more than 1000 km from the source after period-dependent raypath effects are included. Sandanbata et al. (2022) applied the tsunami phase correction method to model dispersive tsunamis from a submarine caldera observed in the deep oceans.

2.6.3 Loading Green's function convolution method

The vertical displacement of the seafloor is equivalent to a change in the depth of the ocean. A static sea surface in equilibrium is an equi-geopotential surface. When the gravitational potential change ϕ' is applied instantaneously and locally to seawater originally in gravitational equilibrium, the seawater flows spontaneously until the final gravitationally balanced geoid surface, which is locally uplifted by ϕ'/g_o from the original sea surface, is achieved. In other words, the geoid height increases by ϕ'/g_o with the additional gravitational potential ϕ'.

By a unit point mass load, the vertical distance between the geoid and the seafloor increases according to (cf. Vinogradova et al. 2015 in which G is defined with an opposite sign of G s in Allgeyer and Cummins (2014) and Baba et al. (2017)):

$$G\left(\boldsymbol{r}',\boldsymbol{r}\right) = G(\alpha) = \frac{a}{M_E}\sum_{l=0}^{\infty}\left(1+k_l'-h_l'\right)P_l(\cos\alpha) \tag{38}$$

where $\boldsymbol{r}$ denotes a location on the surface of the Earth with a point mass located at $\boldsymbol{r}'$. a is the radius of the Earth, M_E is the mass of the Earth, P_l is the lth Legendre polynomial in $\cos\alpha$, α is the angular distance from the point mass, 1 in parentheses represents the gravitational effect of the point mass, k_l' is a Love number representing the additional gravitational effect induced by the gravitational potential of the point mass, and h_l' is a Love number representing the deformation of the Earth by the point mass load. The total increment of the geoid-seafloor distance $\xi(\boldsymbol{r})$ by the distributed tsunami wave amplitude $\eta(\boldsymbol{r})$ on the sea surface is obtained by convolving the Green's function:

$$\begin{aligned}\xi(\boldsymbol{r}) &= \int_S G\left(\boldsymbol{r}',\boldsymbol{r}\right)\left[\eta\left(\boldsymbol{r}'\right)-\xi\left(\boldsymbol{r}'\right)\right]dS \\ &\approx a^2\int_0^{2\pi}d\beta\int_0^{\Delta\alpha}d\alpha G(\alpha)\eta(\alpha,\beta)\cos\alpha\end{aligned} \tag{39}$$

where S is the surface area of the Earth and α and β are colatitude and longitude, respectively, in the coordinate system of $\boldsymbol{r}$. We truncated the convolution of the Green's function to a distance $\Delta\alpha$ in Eq. 39.

In the loading Green's function convolution method, the tsunami wave amplitude is replaced by $\eta-\xi$ and the water depth by $d+\eta-\xi$ in the tsunami computation:

$$\frac{\partial\boldsymbol{u}(\boldsymbol{x},t)}{\partial t} = -g_o\nabla\eta(\boldsymbol{x},t) \tag{40}$$

$$\frac{\partial(\eta(\boldsymbol{x},t)-\xi(\boldsymbol{x},t))}{\partial t} = -\nabla((d(\boldsymbol{x})+\eta(\boldsymbol{x},t))\boldsymbol{u}(\boldsymbol{x},t)) \tag{41}$$

We have assumed that $|\nabla\eta| \gg |\nabla\xi|$. Following the use of the two Green's functions (Sect. 2.4.4) in the ocean tide theory for a deformable Earth (e.g., Hendershott 1972), Allgeyer and Cummins (2014) incorporated the change in the depth of the seafloor induced by the tsunami water mass loading in the finite difference computation of tsunamis. Baba et al. (2017) additionally included the gravitational potential change induced by the tsunami water mass in the tsunami calculations (Eq. 38). In the time-domain tsunami computation, at each time step, the tsunami wave amplitude is used to compute the geoid height change (Eq. 39), and the effective tsunami wave amplitude $\eta-\xi$ is used for the conservation of water mass (Eq. 41). Pre-computed point-mass-load Green's functions are then convolved in the space domain. A new equivalent ocean depth η is calculated and used in the next time step. To reduce the heavy computational cost of convolving two functions on a sphere (Eq. 39), we convolve the two surface functions $G(\alpha)$ and $\eta(\alpha,\beta)$ expanded in the spherical harmonics wavenumber domain, and then the convolution is reduced to a multiplication of two functions in the spherical harmonics

wavenumber domain. At every time step, forward and backward spherical harmonics wavenumber transformations of the tsunami height are computed. Although we reduced the computational cost by replacing the convolution with the multiplication, the convolution part still accounts for ~ 70% of the computation time (Allgeyer and Cummins 2014).

Further investigation of the loading Green's function convolution method is required in two points. The first point is the truncation angle $\Delta\alpha$ for the convolution integration in Eq. 39 (Allgeyer and Cummins 2014). For a tsunami from a very large earthquake with a source dimension of 1400 km (e.g., the 2004 Sumatra–Andaman earthquake), an angle α of 7 degrees is required to cover just one wavelength of the tsunami, and the horizontal scale of the induced deformation of the Earth would be larger. We need to adjust the truncation angle depending on the tsunami problem that we compute. The second point is that the Green's functions are computed assuming that the forced oscillation period ω_o is the frequency of the semidiurnal tide (Sect. 2.4.4). This is a reasonable assumption for tidal problems. For tsunami problems whose wave period is as short as 10 min or less, we need to use the correct Green's function computed at the short tsunami wave period. The period of the semidiurnal tide is ~ 12 h, and the deformation of the Earth at that period is close to the static deformation because the inertia term is neglected. For the forced deformation of the Earth at a period of 10 min, which is within the free oscillation periods of the Earth, we need to evaluate the inertial term, which might be non-negligible.

In ocean tide theory, seawater is treated as an incompressible homogeneous fluid that does not store elastic energy. As Watada (2013) demonstrated, both the density-stratified static seawater due to its compressibility and the dynamic compressibility of seawater slow down the tsunami speed. For long waves, the effect of seawater compressibility on the tsunami phase speed can be included as an ocean depth correction (Sect. 2.5.1). Allgeyer and Cummins (2014) and Baba et al. (2017) included the effect of density stratification of static seawater by hydrostatic pressure but not the effect of the dynamic compressibility, i.e., elastic energy stored in compressible seawater.

3 Impacts on trans-oceanic tsunami studies

In this section, we present examples of how the phase correction method has been utilized in the analysis of tsunamis generated by large earthquakes. Some studies have used the method to adjust tsunami traveltimes, others to improve the quality of tsunami Green's functions for better modeling of earthquake and tsunami sources, and others to reproduce the dispersive wave trains that appear in later phases and cannot be modeled by long-wave theory (Fig. 3). A large number of earthquake and

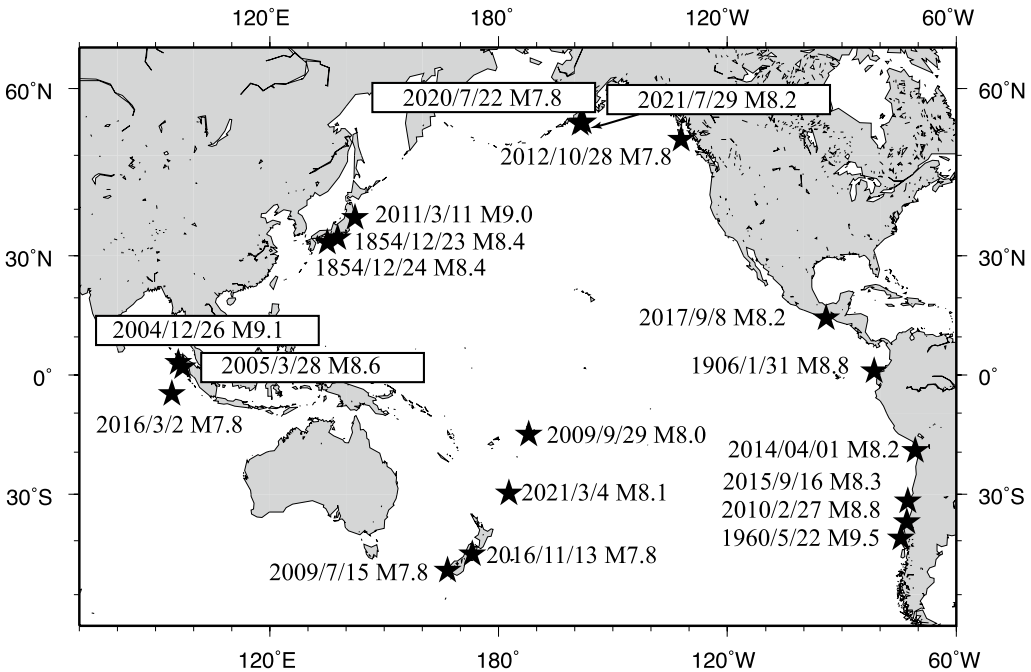

Fig. 9 A map showing tsunamigenic earthquakes to which the new tsunami computation method developed by Watada et al. (2014) has been applied, except for the 2015 Illapel earthquake to which the method developed by Allgeyer and Cummins (2014) has been applied. The figure has been adapted and modified from Fig. 4 of Watada (2021)

tsunami studies have been conducted on the events listed in the following sections. Rather than referring to all of them, I will briefly describe the application of the phase correction method to past tsunami events on the world map in Fig. 9 in reverse chronological order.

3.1 2021 Chignik (Alaska) earthquake M8.2

The earthquake occurred just east of the Shumagin seismic gap, which does not appear to have hosted large historic earthquakes with a magnitude > M7. This event took place east of the Alaska Peninsula along the Aleutian subduction zone. The ocean topography in the area from the peninsula to the trench is characterized by an extended shallow (~ 200 m) continental shelf. The observed tsunami had characteristic long-period (57–73 min) components, which were longer than those generated by megathrust earthquakes of a similar magnitude. Mulia et al. (2022a) attributed the long-period tsunamis to the deeper location of the megathrust earthquake fault, which did not break the shallowest part of the plate boundary along the trench. Large-horizontal-scale sea surface uplift over a shallow ocean produced the long-period tsunamis.

3.2 2021 Raoul Island earthquake M8.1

The earthquake occurred along the Kermadec subduction zone on March 4, 2021, at 19:28 UTC. An M7.4 foreshock occurred at 17:41, deeper and 55 km west of the main M8.1 Raoul Island event. Near New Zealand, there was also an M7.3 earthquake that occurred at 13:27. The recently installed New Zealand DART network recorded three tsunamis. Only the mainshock subfault slips were inverted from the DART records (Romano et al. 2021).

3.3 2020 Shumagin (Alaska) earthquake M7.8

The earthquake occurred within the Shumagin seismic gap, but only ruptured a part of the gap. The ocean topography is also characterized by an extended shallow (~ 200 m) continental shelf extending ~ 150 km offshore (Sect. 3.1). The tsunami, like the 2021 Chignik (Alaska) earthquake, was dominated by the anomalously long-period (~ 60 min) wave components. The tsunami waveform inversion for the fault slip indicates a confined slip at depths of 20–40 km and did not break the up-dip part of the fault near the trench, which would result in short-period tsunamis (Mulia et al. 2022b).

3.4 2017 Tehuantepec earthquake M8.2

Gusman et al. (2018a) investigated the normal fault event that occurred within the subducting Cocos plate beneath Central America by analyzing near-field tide gauge and far-field DART tsunami records. Waveform inversion resolves the optimum sea-surface displacement and infers a compact large slip (3–6 m) at depths between 30 and 90 km in the slab. Zaytsev et al. (2021) confirmed the presence of a small (2–3 cm) but distinct sea-level subsidence preceding the frontal crest wave of a tsunami only at distant stations. Two DART stations located at 1–2 h traveltime away from the source did not show the distinct subsidence before the main crest.

3.5 2016 Kaikoura earthquake M7.8

The 2016 Kaikoura earthquake involved multiple faults on land, onshore, and offshore of the South Island of New Zealand. Gusman et al. (2018b) adopted a two-step inversion scheme to invert fault slips in complex fault geometry. In the first step, subaerial and seafloor displacements were inverted from tsunami waveforms, InSAR, GPS, and coastal uplift data. In the second step, the fault slips were inverted from the surface displacements obtained in the first step. The analyzed tsunami data are tide gauge records along the New Zealand coasts located within a few hours of the source in terms of tsunami traveltimes. The main purpose of applying the phase correction method to these near-field tsunami data is to include the dispersion effect.

3.6 2016 Wharton Basin earthquake M7.8

The DART stations installed in the Indian Ocean recorded small tsunamis from a large strike-slip earthquake that occurred in the middle of the Ninety East Ridge and Sumatra Island, Indonesia. Gusman et al. (2017), by a joint inversion of teleseismic and tsunami waveforms, showed that the earthquake occurred on a north–south striking westward-dipping plane extending 150 km horizontally and 60 km vertically. The inversion indicated bilateral rupture fronts spreading from the epicenter at a speed of 2 km/s.

3.7 2015 Illapel (Chile) earthquake M8.3

Wang et al. (2021) carefully looked into the DART and tide gauge records in the Pacific Basin from the 2015 Illapel earthquake, which generated trans-Pacific tsunamis. The leading negative phase and traveltime delays were confirmed. Using the JAGURS tsunami computation package developed by Baba et al. (2017), they examined the effects of seawater density stratification, SAL, and linear surface gravity on tsunami waveforms and tsunami traveltimes. Among the three effects, SAL is responsible for the leading negative phase, consistent with the discussions in Sects. 2.5.2 and 2.5.3.

3.8 2014 Iquique (Chile) earthquake M8.2

This was the third event that generated trans-Pacific tsunamis after the 2010 Maule (Chile) and 2011 Tohoku-Oki

events. Gusman et al. (2015) confirmed the increase in traveltime delay with increasing traveltime and the initial sea-surface depression in the far-field tsunami waveforms. These effects were incorporated into the synthetic tsunami waveforms by applying the phase correction method to the synthetic long-wave waveforms. They jointly inverted the teleseismic and tsunami waveforms and GPS displacement data for subfault slip kinematics. The largest slip located down dip beneath the coast was well constrained by the tsunami and GPS data, while the moment rate was constrained by the seismic waveform data. The best rupture propagation speed was estimated to be 1.5 km/s.

3.9 2012 Haida Gwaii earthquake M7.8

The earthquake occurred along the trench off the Haida Gwaii archipelago, Canada, where the Pacific plate subducts obliquely beneath the North American plate. The tsunamis from the earthquake were recorded by near-field tide gauges (traveltime < 1 h), mid-field absolute pressure gauges collocated with ocean-bottom seismometers at the deep seafloor (traveltime < 3 h), and far-field DART stations (traveltime < 6 h). The mid- and far-field tsunami waveforms exhibit dispersive characteristics following the leading main pulse. Gusman et al. (2016) applied the dispersive synthetic tsunami Green's functions, which were calculated by the phase correction method for the inversion of the coseismic initial sea-surface elevation. The phase correction method not only reproduces the traveltime delay and initial phase reversal but also generates dispersive later phases (Fig. 3d). Including the dispersion effect in tsunami waveform modeling improves the waveform fit of the later phases after waveform inversion. They proposed a more plausible initial sea-surface elevation model, including a submarine mass failure that might have generated a focused sea-surface peak near the southern end of the Queen Charlotte Fault that runs through the Haida Gwaii archipelago.

3.10 2011 Tohoku-Oki earthquake M9.0

The megathrust earthquake generated tsunamis recorded in and around the Pacific Ocean. Far-field tsunami traveltime delays and initial phase reversals were again observed after the 2011 Maule (Chile) earthquake tsunami and triggered new distant tsunami studies that fundamentally changed the conventional view of long-wave propagation (e.g., Watada et al. 2014; Sect. 2). Ho et al. (2017) improved the phase correction method by including density-stratified seawater in the Earth model and using the minimum tsunami raypath for more accurate phase delay calculations (Sect. 2.6.1). They applied the method to near- and far-field tsunami records to invert the initial sea-surface elevation. With the improved synthetic tsunami Green's function, they showed that the inverted elevation using only far-field (traveltime > 3 h) data is similar to, but smoother than, that using only near-field (traveltime < 3 h) data. Furthermore, the spatial and temporal sea-surface elevation changes during the first 4 min that reflect the spreading slips on the subfaults of the megathrust earthquake can be retrieved by multiple time-window inversions using only the far-field tsunami records. The spatial and temporal evolution of the sea-surface elevation obtained from only far-field records shows an initial large sea-surface rise increasing toward the trench followed by migration along the trench, which is consistent with the result obtained from only near-field records.

3.11 2010 Maule (Chile) earthquake M8.8

The event generated trans-Pacific tsunamis that were systematically recorded for the first time near the source (traveltime ~ 3 h) and at far field (traveltime ~ 23 h) by the DART network (Sect. 2.2). Because of the tsunami traveltime delays in the observed far-field DART records relative to the long-wave simulations, Fujii and Satake (2013) analyzed only near-field tide gauge records near South America, DART records (traveltime < 10 h), coseismic GPS data, and coastal leveling data for the subfault slip inversion by using conventional long-wave synthetic tsunami Green's functions. The fault slip model estimated by inversions using only tsunami data and the model by joint inversions using tsunami and geodetic data both show similar largest slips at the deepest subfaults (> 24 km) beneath the coastline, in contrast to the shallow offshore slip asperities revealed by other seismic waveform studies.

It turned out that the tsunami records, even at 10 h from the tsunami source, could not be modeled for fault slips by conventional long-wave tsunami theory. The faster propagation speed of the conventional long-wave tsunami relative to the real tsunami speed erroneously placed the fault slips to be away from the DART stations offshore, i.e., large fault slips were estimated at the down dip of the faults. Yoshimoto et al. (2016) reanalyzed the same dataset using the new synthetic tsunami Green's functions computed by the phase correction method. Three inversion results from near-field tsunami records only (traveltime < 10 h), far-field tsunami records only (traveltime > 10 h), and joint tsunami and geodetic data show similar slip patterns, with large slips concentrated along the trench, which are consistent with other seismic and geodetic studies.

3.12 2009 Samoa earthquake M8.0

The earthquake mechanism has been debated as to whether the source is a doublet composed of a Tonga Trench megathrust event and an outer rise normal fault event or a single outer rise event. Hossen et al. (2018) applied the GFTR method to local tide gauges and DART records surrounding the tsunami source region to invert the initial sea-surface elevation. The recovered elevation map was consistent with the doublet source. The obtained sea-surface elevation was inverted for the slip distribution on the fault and the dip orientation of the normal fault. The phase correction method was used to determine the traveltime calibration for a given station distance from the source. Traveltime adjustment of the Green's functions was applied to far-field DART station records.

3.13 2009 Dusky Sound earthquake M7.8

The earthquake occurred offshore the South Island of New Zealand near the transition corner of the plate boundary between the Pacific-Australian plate boundary from the strike-slip Alpine fault to the Puysegur trench. The shallow dipping fault with a small dip angle generated a tsunami that was recorded by coastal tide gauges and two DART stations, as well as the DPG temporal array deployed west of the South Island. Sheehan et al. (2019) applied the phase correction method to the local tsunami Green's functions computed by solving the linear shallow-water wave equation to include the wave dispersion effect for the slip inversion of the subfaults.

3.14 2005 Nias earthquake M8.6

The megathrust earthquake was an aftershock that occurred south of the 2004 Sumatra–Andaman earthquake. The tsunami waveforms were recorded by coastal tide gauges in and around the Indian Ocean. Fujii et al. (2020) applied the phase correction to the tsunami Green's functions to include the elastic and gravitational coupling effects. The subfault slip inversion revealed a diffuse slip (~2 m over an area of 400 km×100 km) at deeper parts (20–54 km) of the fault, with a large localized slip (7 m over 100 km×100 km). Compared to the seismic magnitude, the earthquake generated relatively small tsunamis. The large slips in the deeper parts of the fault were responsible for the small tsunami generation. The obtained slip distribution is similar to that obtained from the local geodetic and GPS network data, indicating that the far-field tsunami waveforms, once corrected by the phase correction method, have a resolving power of the fault slips comparable to the local geodetic data.

3.15 2004 Sumatra–Andaman earthquake M9.1

The source area of the 2004 Sumatra–Andaman earthquake, which occurred along the Sunda Trench, extends 1400 km from off the northwest coast of Sumatra, Indonesia, to the Andaman Islands, India (Fujii et al. 2021). The tsunami struck the coasts surrounding the Indian Ocean, making it the most disastrous tsunami of the last century. Titov et al. (2005) and Rabinovich et al. (2017), by examining the running spectrum of tide gauge and DART records in the Pacific Ocean after the 2004 Sumatra–Andaman earthquake, argued that two tsunamis, one that circled southern Australia, and one that passed through the Atlantic Ocean and the Drake Passage, entered the Pacific Ocean. Fujii et al. (2021) computed the westward and eastward tsunami propagations separately from the Sumatra–Andaman earthquake source region to the Pacific Ocean using the phase correction method after measuring the raypath lengths of the two tsunami propagation paths of the minimum tsunami traveltime. By comparing the synthetic and observed tsunami waveforms, they found that an isolated wave packet recorded 36 h after the earthquake at two DART stations off the western coast of North America was a tsunami propagated eastward from the source region.

3.16 1960 Valdivia (Chile) earthquake M9.5

The 1960 Valdivia (Chile) earthquake occurred over an area of extending 800 km along the Nazca subduction

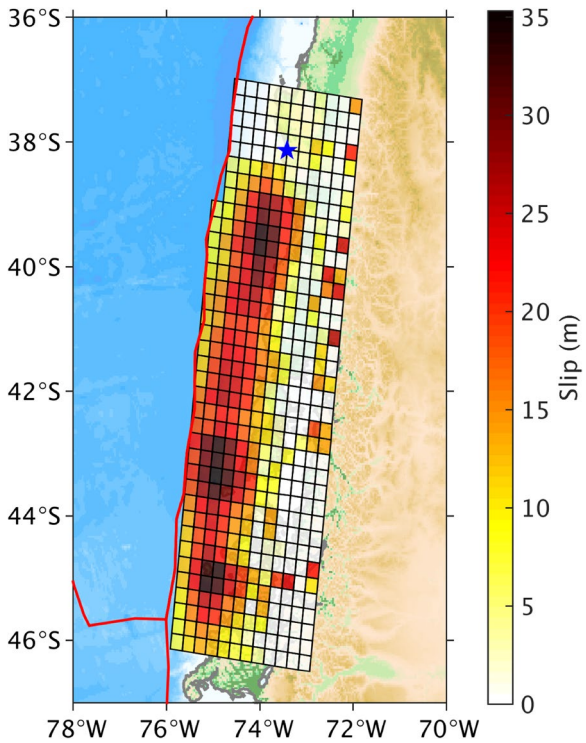

Fig. 10 Finite fault-slip distribution of the 1960 Chilean earthquake estimated by a joint inversion of the far-field tsunami records and local geodetic data. The figure has been adaptedi and modified from Fig. 13 of Ho et al. (2019)

zone beneath South America (Ho et al. 2019). The source area is just south of the 2010 Maule (Chile) earthquake source area (Satake et al 2020). Fujii and Satake (2013) used tide gauge records (traveltime < 6 h) only in South America because of the traveltime delay problem, leveling data near the source area, and sea-level change data along the coast for the subfault slip inversion using conventional long-wave synthetic tsunami Green's functions. As we have seen for the 2010 Maule (Chile) earthquake subfault analysis in Sect. 3.11, the fault slip model estimated by inversions using only tsunami data shows the largest slips at the deepest (> 34 km) subfaults beneath the coastline, whereas the model estimated by joint inversions using tsunami and geodetic data shows the largest slips in the middle of the subfaults (17–34 km). Ho et al. (2019) jointly inverted all tsunami waveforms recorded by tide gauges in the Pacific and the same local geodetic data used by Fujii and Satake (2013) for the subfault slip model using the new synthetic tsunami Green's functions and found three major asperities offshore close to the trench (Fig. 10). Ho et al. (2019) took full advantage of the fast computation time of the phase correction method to calculate the Green's functions for the 435 subfaults.

3.17 1906 Ecuador–Colombia earthquake M8.8

The event occurred along the upper boundary of the subducting Nazca plate beneath the South American plate. Because of the active seismicity in the source area after the event, such as events with M7.8 in 1942, M7.6 in 1958, M8.1 in 1979, and M7.8 in 2016, the detailed distribution of the slip deficit, or interplate coupling, along the subducting plate interface has been the subject of active study. A major limitation in these discussions has been the poorly known slip distribution of the largest 1906 event. In the papers cited in this subsection, the phase correction method allows us to simulate far-field tsunami records.

There are far-field tide gauge tsunami records, two in North America (traveltime ~ 11 h), one in Honolulu (~ 12 h), and four in Japan (~ 20 h), one in Panama (~ 2 h). Yoshimoto et al. (2017) analyzed the Honolulu, San Francisco, and Ayukawa records and obtained a subfault slip model with concentrated slip regions near the trench, which do not overlap with the large slip regions of the 1942, 1958, 1979, and 2016 events. Yamanaka and Tanioka (2021) analyzed Panama, San Diego, and four records in Japan, after calibrating the timing of the tsunami records by comparing them with the astronomical tides. They obtained a subfault slip model with large slips in the north of the event source region, which overlaps the slip region of the 1979 event, and less slips which overlap the slip regions of the other three events.

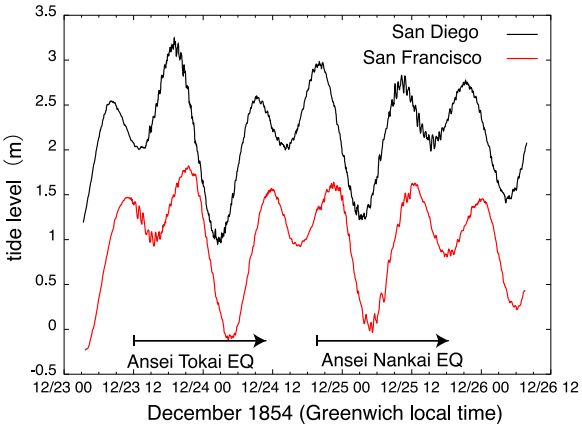

Fig. 11 Two tide gauge records at San Diego and San Francisco, the USA. Two tsunamis from the 1854 Tokai and Nankai earthquakes occurred offshore Japan, were recorded in one trace. The San Diego record is shifted by 1.5 m for better visibility. Original numerical data are available from Kusumoto et al. (2020). The figure has been adapted and modified from Fig. 5 of Watada (2021)

Yamanaka and Tanioka (2018) confirmed that the simulated Honolulu tide gauge record was consistent with the observed record. The three tsunami waveform modeling studies cited in this subsection indicate that the seismic moment of the 1906 event is between M8.2 and M8.6.

3.18 1854 Ansei great earthquakes (two M8.4)

On December 23, 1854, the first great earthquake struck off the coast of Tokai along the southern coast of Japan. About 30 h later, the second great earthquake struck west of the first one off the Nankai region along the southern coast of Japan. Two earthquakes occurred along the upper boundary of the subducting Philippine Sea plate beneath Honshu Island, Japan.

Tsunamis generated by the two earthquakes traveled across the Pacific Ocean and were recorded by three tide gauges at Astoria, San Francisco, and San Diego, in the USA (Kusumoto et al. 2020, Fig. 11). The astronomical tides were used to calibrate the timing of the records. The earthquake origin time, which is only available in documents in Japan (e.g., Sugimori et al. 2022), was estimated from the arrival times in the tsunami waveforms of the Ansei Tokai earthquake simulated by using the phase correction method or the loading Green's function convolution method. Kusumoto et al. (2020) confirmed that the two methods calculate exactly the same traveltimes. A small waveform difference appeared only in the later phases (Fig. 4 of Kusumoto et al. 2020). The time difference between two earthquakes was measured from the tide gauge records in San Francisco and San Diego (Kusumoto et al. 2022).

4 Conclusions

The development of deep ocean tsunami observation systems in the Pacific Ocean has provided high-quality tsunami records generated by the 2010 Maule (Chile) and 2011 Tohoku-Oki earthquakes without coastal interference. These data have recorded the waveform evolution as the tsunami spread throughout the entire Pacific, revealing that conventional tsunami theory is unable to explain not only the delayed traveltimes but also the initial phase reversal of the observed distant tsunami waveforms. The discrepancy between theory and observation has led to the development of a tsunami propagation theory that eliminates the assumptions in the conventional tsunami theory and to the establishment of methods for computing a tsunami for a gravitationally coupled elastic Earth system. Based on the new tsunami theory, two equivalent tsunami synthetic methods, the phase correction method by Watada et al. (2014) and the loading Green's function convolution method by Allgeyer and Cummins (2014), have been developed.

The computed tsunami waveforms using the new methods reproduce the observed waveforms in the far field, including the traveltime delays and the initial phase reversal. The traveltime delay is due to the slowdown of the tsunami phase speed by the compressible seawater, elastic solid Earth, and the gravitational potential change during tsunami propagation. The latter two also cause the reverse dispersion of a tsunami, i.e., slower tsunami phase velocities for wave periods longer than 1000 s, resulting in the initial phase reversal of a distant tsunami. The new tsunami synthetic methods greatly diminish the waveform and traveltime differences between the observed and simulated distant tsunamis.

The new distant tsunami waveform calculation methods make it possible to determine the slip distribution of large earthquakes from far-field tsunami records. Past distant tsunami events recorded by coastal tide gauges, which had not been studied by conventional simulation methods because of the traveltime and waveform mismatch problems, have become the subject of quantitative tsunami studies using the waveforms. Distant tsunami synthetic methods have been applied to more than 19 earthquake tsunamis since the first trans-Pacific tsunami records in 1854 and have successfully quantified the earthquake slip models. Analyses of distant tsunami records are elucidating the slip distributions of past giant earthquakes under the seafloor, and the fault slip history of repeating giant shallow thrust earthquakes is gradually being revealed.

Abbreviations

BPR	Bottom pressure recorder
DART	Deep-ocean Assessment Reporting of Tsunamis
DONET	Dense Oceanfloor Network system for Earthquakes and Tsunamis
DPG	Differential pressure gauge
ERI	Earthquake Research Institute of the University of Tokyo
FFT	Fast Fourier transform
GEOSS	Global Earth Observation System of Systems
GFTR	Green's function-based time reverse imaging
HSLDE	Homogeneous simultaneous linear differential equation
IFFT	Inverse fast Fourier transform
JAMSTEC	Japan Agency for Marine-Earth Science and Technology
JMA	Japan Meteorological Agency
MLIT	Ministry of Land, Infrastructure, Transport and Tourism, Japan
NIED	National Research Institute for Earth Science and Disaster Resilience
NOWPHAS	Nationwide Ocean Wave information network for Ports and HArbourS
NOAA	National Oceanic and Atmospheric Administration
OBPG	Ocean-bottom pressure gauge
PREM	Preliminary reference Earth model
RTK-GPS	Real-time kinematic global positioning system
SAL	Self-attraction and loading
SLDE	Simultaneous linear differential equation
SMF	Submarine mass failure
S-net	Seafloor observation network for earthquakes and tsunamis along the Japan Trench

Acknowledgements

The author thanks the Editor for kindly guiding the PEPS submission process through the online editorial manager. The author appreciates valuable comments by two reviewers.

Author contributions

SW proposed the topic, conceived and designed the review, wrote the manuscript, and selected and prepared the figures. The author read and approved the final manuscript.

Funding

This work was supported by JSPS KAKENHI Grant Numbers 19K04034 and 21K21353.

Availability of data and materials

The original numerical data in Fig. 11 are available from the supplementary information of Kusumoto et al. (2020). Programs to compute tsunami normal modes for a spherically symmetric Earth model are available at https://github.com/WatadaShingo/mode-tsunami. Examples of simulation and phase correction for a dispersive tsunami are available at https://github.com/WatadaShingo/tsunami-1d.

Declarations

Competing interests

The authors declare that they have no competing interest.

Received: 26 September 2022 Accepted: 23 April 2023
Published online: 22 May 2023

References

Abdolali A, Kadri U, Kirby JT (2019) Effect of water compressibility, sea-floor elasticity, and field gravitational potential on tsunami phase speed. Sci Rep 9:16874. https://doi.org/10.1038/s41598-019-52475-0

Allgeyer S, Cummins P (2014) Numerical tsunami simulation including elastic loading and seawater density stratification. Geophys Res Lett 41:2368–2375. https://doi.org/10.1002/2014GL059348

Alterman Z, Jarosch H, Pekeris CL (1959) Oscillations of the Earth. Proc Roy Soc Lond Ser Math Phys Sci 252(1268):80–95
Aoi S, Asano Y, Kunugi T, Kimura T, Uehira K, Takahashi N, Ueda H, Shiomi K, Matsumoto T, Fujiwara H (2020) MOWLAS: NIED observation network for earthquake, tsunami and volcano. Earth Planets Space 72:126. https://doi.org/10.1186/s40623-020-01250-x
Baba T, Takahashi N, Kaneda Y, Ando K, Matsuoka D, Kato T (2015) Parallel implementation of dispersive tsunami wave modeling with a nesting algorithm for the 2011 Tohoku tsunami. Pure Appl Geophys 172(12):3455–3472. https://doi.org/10.1007/s00024-015-1049-2
Baba T, Allgeyer S, Hossen J, Cummins PR, Tsushima H, Imai K, Yamashita K, Kato T (2017) Accurate numerical simulation of the far-field tsunami caused by the 2011 Tohoku earthquake, including the effects of Boussinesq dispersion, seawater density stratification, elastic loading, and gravitational potential change. Ocean Model 111:46–54. https://doi.org/10.1016/j.ocemod.2017.01.002
Comer RP (1984) The tsunami mode of a flat earth and its excitation by earthquake sources. Geophys J R Astron Soc 77(1):1–27
Cowling TG (1941) The non-radial oscillations of polytropic stars. Mon Not R Astron Soc 101(8):367–375. https://doi.org/10.1093/mnras/101.8.367
Dawson TH (1978) Wave propagation over a deformable sea floor. Ocean Eng 5(4):227–234
Dingemans MW (1997a) Water wave propagation over uneven bottoms: Linear wave propagation, vol 13. World Scientific, Singapore
Dingemans MW (1997b) Water wave propagation over uneven bottoms: Nonlinear wave propagation, vol 13. World Scientific, Singapore
Dziewonski AM, Anderson DL (1981) Preliminary reference Earth model. Phys Earth Planet Inter 25:297–356
Eckart C (1960) Hydrodynamics of oceans and atmospheres. Pergamon Press, Oxford
Farrell WE (1972) Deformation of the Earth by surface loads. Rev Geophys 10(3):761–797. https://doi.org/10.1029/RG010i003p00761
Fujii Y, Satake K (2013) Slip distribution and seismic moment of the 2010 and 1960 Chilean earthquakes inferred from tsunami waveforms and coastal geodetic data. Pure Appl Geophys 170:1493–1509. https://doi.org/10.1007/s00024-012-0524-2
Fujii Y, Satake K, Watada S, Ho T-C (2020) Slip distribution of the 2005 Nias earthquake (Mw 8.6) inferred from geodetic and far-field tsunami data. Geophys J Int 223(2):1162–1171. https://doi.org/10.1093/gji/ggaa384
Fujii Y, Satake K, Watada S, Ho T-C (2021) Re-examination of slip distribution of the 2004 Sumatra-Andaman earthquake (Mw 9.2) by the inversion of tsunami data using green's functions corrected for compressible seawater over the elastic earth. Pure Appl Geophys 178:4777–4796. https://doi.org/10.1007/s00024-021-02909-6
Gusman AR, Murotani S, Satake K, Heidarzadeh M, Gunawan E, Watada S, Schurr B (2015) Fault slip distribution of the 2014 Iquique, Chile, earthquake estimated from ocean-wide tsunami waveforms and GPS data. Geophys Res Lett 42:1053–1060. https://doi.org/10.1002/2014GL062604
Gusman AR, Mulia IE, Satake K, Watada S, Heidarzadeh M, Sheehan AF (2016) Estimate of tsunami source using optimized unit sources and including dispersion effects during tsunami propagation: the 2012 Haida Gwaii earthquake. Geophys Res Lett 43:9819–9828. https://doi.org/10.1002/2016GL070140
Gusman AR, Satake K, Harada T (2017) Rupture process of the 2016 Wharton Basin strike-slip faulting earthquake estimated from joint inversion of teleseismic and tsunami waveforms. Geophys Res Lett 44:4082–4089. https://doi.org/10.1002/2017GL073611
Gusman AR, Mulia IE, Satake K (2018a) Optimum sea surface displacement and fault slip distribution of the 2017 Tehuantepec earthquake (Mw 8.2) in Mexico estimated from tsunami waveforms. Geophys Res Lett 45:646–653. https://doi.org/10.1002/2017GL076070
Gusman AR, Satake K, Gunawan E, Hamling I, Power W (2018b) Contribution from multiple fault ruptures to tsunami generation during the 2016 Kaikoura Earthquake. Pure Appl Geophys 175:2557–2574. https://doi.org/10.1007/s00024-018-1949-z
Hébert H, Reymond D, Krien Y, Vergoz J, Schindelé F, Roger J, Loevenbruck A (2009) The 15 August 2007 Peru earthquake and tsunami: influence of the source characteristics on the tsunami heights. Pure Appl Geophys 166:211–232. https://doi.org/10.1007/s00024-008-0439-0
Hendershott MC (1972) The effects of solid earth deformation on global ocean tides. Geophy J Int 29(4):389–402
Ho T-C, Satake K, Watada S (2017) Improved phase corrections for transoceanic tsunami data in spatial and temporal source estimation: application to the 2011 Tohoku earthquake. J Geophys Res Solid 122:10155–10175. https://doi.org/10.1002/2017JB015070
Ho T-C, Satake K, Watada S, Fujii Y (2019) Source estimate for the 1960 Chile earthquake from joint inversion of geodetic and transoceanic tsunami data. J Geophys Res Solid 124:2812–2828. https://doi.org/10.1029/2018JB016996
Hossen MJ, Gusman AR, Satake K, Cummins PR (2018) An adjoint sensitivity method applied to time reverse imaging of tsunami source for the 2009 Samoa earthquake. Geophys Res Lett 45:627–636. https://doi.org/10.1002/2017GL076031
Iio Y (1995) Observations of the slow initial phase generated by microearthquakes: implications for earthquake nucleation and propagation. J Geophys Res Solid 100:15333–15349. https://doi.org/10.1029/95JB01150
Imamura F, Nagano O, Goto T, Shuto N (1987) Trans-oceanic tsunami propagation computation for the 1960 Chilean tsunami [in Japanese]. Proc Coast Eng 34:172–176
Imamura F, Shuto N, Goto T (1990) Study on numerical simulation of the Transoceanic propagation of tsunami Part 2: Characteristics of tsunami propagating over the Pacific [in Japanese]. Zisin 43:389–402
Inazu D, Saito T (2013) Simulation of distant tsunami propagation with a radial loading deformation effect. Earth Planets Space 65:835–842. https://doi.org/10.5047/eps.2013.03.010
Kato T, Terada T, Ito K, Hattori R, Abe T, Miyake T, Koshimura S, Nagai T (2005) Tsunami due to the 5 September 2004 off the Kii Peninsula Earthquake, Japan, recorded by a new GPS buoy. Earth Planets Space 57:297–301
Kato T, Terada Y, Nishimura H, Nagai T, Koshimura S (2011) Tsunami records due to the 2010 Chile Earthquake observed by GPS buoys established along the Pacific coast of Japan. Earth Planets Space 63(6):e5–e8. https://doi.org/10.5047/eps.2011.05.001
Kawai H, Satoh M, Miyata M, Kobayashi T (2012) 2010 Chilean Tsunami Observed on Japanese Coast by NOWPHAS GPS Buoys, Seabed Wave Gauges and Coastal Tide Gauges. Int J Offshore Polar Eng 22(3):177–185
Kawai H, Satoh M, Kawaguchi K, Seki K (2013) Characteristics of the 2011 Tohoku tsunami waveform acquired around Japan by NOWPHAS equipment. Coast Eng J 55(3):1350008-1–1350008-27. https://doi.org/10.1142/S0578563413500083
Kimura T, Tanaka S, Saito T (2013) Ground tilt changes in Japan caused by the 2010 Maule, Chile, earthquake tsunami. J Geophys Res Solid 118:406–415. https://doi.org/10.1029/2012JB009657
Kusumoto S, Imai K, Obayashi R, Hori T, Takahashi N, Ho T-C, Uno K, Tanioka Y, Satake K (2020) Origin time of the 1854 Ansei–Tokai tsunami estimated from tide gauge records on the west coast of North America. Seismo Res Lett 91:2624–2630. https://doi.org/10.1785/0220200068
Kusumoto S, Imai K, Hori T (2022) Time difference between the 1854 CE Ansei-Tokai and Ansei–Nankai earthquakes estimated from distant tsunami waveforms on the west coast of North America. Prog Earth Planet Sci 9:2. https://doi.org/10.1186/s40645-021-00458-z
Matsuzawa T (1950) Seismology in Japanese. Kadokawa Shoten, Tokyo
Mulia IE, Gusman AR, Heidarzadeh M, Satake K (2022a) Sensitivity of tsunami data to the up-dip extent of the July 2021 Mw 8.2 Alaska Earthquake. Seismol Res Lett 93(4):1992–2003. https://doi.org/10.1785/0220210359
Mulia IE, Heidarzadeh M, Satake K (2022b) Effects of depth of fault slip and continental shelf geometry on the generation of anomalously long-period tsunami by the July 2020 Mw 7.8 Shumagin (Alaska) earthquake. Geophys Res Lett 49:e2021GL094937. https://doi.org/10.1029/2021GL094937
Nakamura K (1961) Velocity of long gravity waves in the ocean. Sci Reports Tohoku Univ 5th Ser Geophys 13(3):164–173
Okal EA (1982) Mode-wave equivalence and other asymptotic problems in tsunami theory. Phys Earth Planet Inter 30:1–11. https://doi.org/10.1016/0031-9201(82)90123-6
Ozawa S, Nishimura T, Suito H, Kobayashi K, Tobita M, Imakiire T (2011) Coseismic and postseismic slip of the 2011 magnitude-9 Tohoku-Oki earthquake. Nature 475:373–376. https://doi.org/10.1038/nature10227
Rabinovich AB, Woodworth PL, Titov VV (2011) Deep-sea observations and modeling of the 2004 Sumatra tsunami in Drake Passage. Geophys Res Lett 38:L16604. https://doi.org/10.1029/2011GL048305
Rabinovich AB, Thomson RE, Fine IV (2013) The 2010 Chilean tsunami off the west coast of Canada and the northwest coast of the United

States. Pure Appl Geophys 170:1529–1565. https://doi.org/10.1007/s00024-012-0541-1
Rabinovich AB, Titov VV, Moore CW, Eblé MC (2017) The 2004 Sumatra Tsunami in the Southeastern Pacific Ocean: New global insight from observations and modeling. J Geophys Res Oceans 122:7992–8019. https://doi.org/10.1002/2017JC013078
Romano F, Gusman AR, Power W, Piatanesi A, Volpe M, Scala A, Lorito S (2021) Tsunami source of the 2021 MW 81 Raoul Island earthquake from DART and tide-gauge data inversion. Geophys Res Lett 48:e2021GL094449. https://doi.org/10.1029/2021GL094449
Saito T, Matsuzawa T, Obara K, Baba T (2010) Dispersive tsunami of the 2010 Chile earthquake recorded by the high-sampling-rate ocean-bottom pressure gauges. Geophys Res Lett 37:L23303. https://doi.org/10.1029/2010GL045290
Sandanbata O, Watada S, Ho T-C, Satake K (2021) Phase delay of short-period tsunamis in the density-stratified compressible ocean over the elastic Earth. Geophys J Int 226(3):1975–1985. https://doi.org/10.1093/gji/ggab192
Sandanbata O, Watada S, Satake K, Kanamori H, Rivera L, Zhan Z (2022) Sub-decadal volcanic tsunamis due to submarine trapdoor faulting at Sumisu caldera in the Izu-Bonin Arc. J Geophys Res Solid 127:e2022JB024213. https://doi.org/10.1029/2022JB024213
Satake K (2015) Tsunamis. In: Schubert G (ed) Treatise on geophysics, vol 4. Elsevier, Amsterdam, Netherlands, pp 477–504. https://doi.org/10.1016/B978-044452748-6.00078-X
Satake K, Heidarzadeh M, Quiroz M, Cienfuegos R (2020) History and features of trans-oceanic tsunamis and implications for paleo-tsunami studies. Earth-Sci Rev 202:103112. https://doi.org/10.1016/j.earscirev.2020.103112
Sells CL (1965) The effect of a sudden change of shape of the bottom of a slightly compressible ocean. Phil Trans Royal Soc Lond Ser A 258(1092):495–528. https://doi.org/10.1098/rsta.1965.0049
Sheehan AF, Gusman AR, Satake K (2019) Improving forecast accuracy with tsunami data assimilation: the 2009 Dusky Sound, New Zealand, tsunami. J Geophys Res Solid 124:566–577. https://doi.org/10.1029/2018JB016575
Stoneley R (1963) The propagation of tsunamis. Geophys J Int 8(1):64–81
Sugimori R, Ariizumi K, Satake K (2022) Origin time of the 1854 Tokai earthquake recorded in the Logbook of the Russian Frigate Diana. J Disaster Res 17(3):409–419. https://doi.org/10.20965/jdr.2022.p0409
Sulzbach R, Dobslaw H, Thomas M (2021) High-resolution numerical modeling of barotropic global ocean tides for satellite gravimetry. J Geophy Res Oceans 126:e20200JC17097. https://doi.org/10.1029/2020JC017097
Takahashi M (1981) Telemetry bottom pressure observation system at a depth of 2,200 meter. J Phys Earth 29:77–88
Takeuchi H, Saito M (1972) Seismic surface waves. Methods Comput Phys 11:217–295
Tappin DR, Grilli ST, Harris JC, Geller RJ, Masterlark T, Kirby JT, Shi F, Ma G, Thingbaijam KKS, Mai PM (2014) Did a submarine landslide contribute to the 2011 Tohoku tsunami? Mar Geol 357:344–361. https://doi.org/10.1016/j.margeo.2014.09.043
Titov V, Rabinovich AB, Mofjeld HO, Thomson RE, González FI (2005) The global reach of the 26 December 2004 Sumatra tsunami. Science 309(5743):2045–2048. https://doi.org/10.1126/science.1114576
Tsai VC, Ampuero J-P, Kanamori H, Stevenson DJ (2013) Estimating the effect of Earth elasticity and variable water density ontsunami speeds. Geophys Res Lett 40:492–496. https://doi.org/10.1002/grl.50147
Tsushima H, Ohta Y (2014) Review on near-field tsunami forecasting from offshore tsunami data and onshore GNSS data for tsunami early warning. J Disaster Res 9(3):339–357. https://doi.org/10.20965/jdr.2014.p0339
Vinogradova NT, Ponte RM, Quinn KJ, Tamisiea ME, Campin J, Davis JL (2015) Dynamic adjustment of the ocean circulation to self-attraction and loading effects. J Phys Oceanogr 45(3):678–689. https://doi.org/10.1175/JPO-D-14-0150.1
Wang DL (2015) An ocean depth-correction method for reducing model errors in tsunami travel time: application to the 2010 Chile and 2011 Tohoku tsunamis. Sci Tsunami Hazards 34(1):1–22
Wang P, Ren Z, Sun L, Hou J, Wang Z, Yuan Ye YuF (2021) Observations and modelling of the travel time delay and leading negative phase of the 16 September 2015 Illapel, Chile tsunami. Acta Oceanol Sin 40:11–30. https://doi.org/10.1007/s13131-021-1830-2
Wang P, Sun L, Zhao L (2022) An efficient method to improve travel time delays of transoceanic tsunamis based on depth-correction scheme. Ocean Dyn 72:477–494. https://doi.org/10.1007/s10236-022-01514-y
Ward SN (1980) Relationships of tsunami generation and an earthquake source. J Phys Earth 28:441–474. https://doi.org/10.4294/jpe1952.28.441
Watada S (2013) Tsunami speed variations in density-stratified compressible global oceans. Geophys Res Lett 40:4001–4006. https://doi.org/10.1002/grl.50785
Watada S (2021) Tsunamis shake the Earth—improvement of distant tsunami waveform analysis technology—[in Japanese]. Eartqhuake J 71:60–65
Watada S, Kanamori H (2010) Acoustic resonant oscillations between the atmosphere and the solid earth during the 1991 Mt. Pinatubo Eruption. J Geophys Res Solid 115:B12319. https://doi.org/10.1029/2010JB007747
Watada S, Kusumoto S, Satake K (2014) Traveltime delay and initial phase reversal of distant tsunamis coupled with the self-gravitating elastic Earth. J Geophy Res Solid 119(5):4287–4310. https://doi.org/10.1002/2013JB010841
Wei Y, Bernard EN, Tang L, Weiss R, Titov VV, Moore C, Spillane M, Hopkins M, Kânoğlu U (2008) Real-time experimental forecast of the Peruvian tsunami of August 2007 for U.S. coastlines. Geophys Res Lett 35:L04609. https://doi.org/10.1029/2007GL032250
Yamamoto T (1982) Gravity waves and acoustic waves generated by submarine earthquakes. J Soil Dyn Earthquake Eng 1:75–82. https://doi.org/10.1016/0261-7277(82)90016-X
Yamanaka Y, Tanioka Y (2018) Large amplification of the 1906 Colombia–Ecuador earthquake tsunami in Hilo Bay induced by bay-scale resonance. Geophys J Int 214(3):1937–1946. https://doi.org/10.1093/gji/ggy244
Yamanaka Y, Tanioka Y (2021) Study on the 1906 Colombia–Ecuador megathrust earthquake based on tsunami waveforms observed at tide gauges: release variation of accumulated slip deficits in the source area. J Geophys Res Solid 126:e2020JB021375. https://doi.org/10.1029/2020JB021375
Yamazaki Y, Lay T, Cheung KF, Yue H, Kanamori H (2011) Modeling near-field tsunami observations to improve finite-fault slip models for the 11 March 2011 Tohoku earthquake. Geophys Res Lett 38:L00G15. https://doi.org/10.1029/2011GL049130
Yoshimoto M et al (2017) Depth-dependent rupture mode along the Ecuador–Colombia subduction zone. Geophys Res Lett 44:2203–2210. https://doi.org/10.1002/2016GL071929
Yoshimoto M, Watada S, Fujii Y, Satake K (2016) Source estimate and tsunami forecast from far-field deep-ocean tsunami waveforms—the 27 February 2010 Mw 8.8 Maule earthquake. Geophys Res Lett 43:659–665. https://doi.org/10.1002/2015GL067181
Zaytsev O, Rabinovich AB, Thomson RE (2021) The impact of the Chiapas Tsunami of 8 September 2017 on the coast of Mexico. Part 1: observations, statistics, and energy partitioning. Pure Appl Geophys 178:4291–4323. https://doi.org/10.1007/s00024-021-02893-x
Zetler BD, Symons JM (1961) The tsunami of May 22, 1960 as recorded at tide stations: preliminary report. U.S. Dept. of Commerce, Coast and Geodetic Survey, Washington, D.C.
Japan Meteorological Agency (2010) The sixth meeting of the study group for tsunami forecast technology.https://www.data.jma.go.jp/svd/eqev/data/study-panel/tsunami/benkyokai6/index.html (in Japanese) Accessed Sep 2022
Mallard WW, Dalrymple RA (1977) Water waves propagating over a deformable bottom. paper presented at 9th Annual Offshore, Technology Conference, Houston, Texas, 1977
Meinig C, Stalin S E, Nakamura AI, Milburn HB (2005) Real-time Deep-ocean tsunami measuring, monitoring, and reporting system: the NOAA DART II description and disclosure, pp 1–15
Nakamura K, Watanabe H (1961) Tsunami forerunner observed in case of the Chile Tsunami of 1960. In: Report on the Chilean Tsunami of May 24, 1960, as Observed Along the Coast of Japan. The committee for field investigation of the Chilean tsunami of 1960

Publisher's Note